Beyond the Ionic Radii: A Multifaceted Approach to Understand Differences between the Structures of *Ln*NbO_4 and *Ln*TaO_4 Fergusonites

Bryce G. Mullens[1], Matilde Saura-Múzquiz[1,2], Frederick P. Marlton[1], Maxim Avdeev[1,3], Helen E. A. Brand[4], S. Mondal[5], G. Vaitheeswaran[6,*], and Brendan J. Kennedy[1,*]

[1] School of Chemistry, The University of Sydney, Sydney, New South Wales 2006, Australia

[2] Current Address: Department of Materials Physics, Universidad Complutense de Madrid, 28040, Madrid, Spain

[3] Australian Nuclear Science and Technology Organisation, Lucas Heights, New South Wales 2234, Australia

[4] Australian Synchrotron, Australian Nuclear Science and Technology Organisation, 800 Blackburn Road, Clayton, Victoria 3168, Australia

[5] Advanced Centre of Research in High Energy Materials (ACRHEM), University of Hyderabad, Prof. C. R. Rao Road, Gachibowli, Hyderabad 500 046, Telangana, India

[6] School of Physics, University of Hyderabad, Prof. C. R. Rao Road, Gachibowli, Hyderabad 500 046, Telangana, India

[*] Corresponding Authors: Brendan J. Kennedy (brendan.kennedy@sydney.edu.au), G. Vaitheeswaran (vaithee@uohyd.ac.in)

Abstract

Synchrotron X-ray powder diffraction methods have been used to obtain accurate structures of the lanthanoid tantalates, *Ln*TaO_4, at room temperature. Three different structures are observed, depending on the size of the *Ln* cation: $P2_1/c$ (*Ln* = La, Pr), $I2/a$ (*Ln* = Nd-Ho), and $P2/c$ (*Ln* = Tb-Lu). BVS analysis indicated that Ta^V is six-coordinate in these structures, with four short bonds and two longer bonds. Synchrotron X-ray powder diffraction methods were also used to observe the impact of Ta doping on the orthoniobates, *Ln*$(Nb_{1-x}Ta_x)O_4$ (*Ln* = Pr, Nd, Sm, Gd, Tb, Dy, Ho, Yb and Lu). Where both the niobate and tantalate oxide were isostructural (fergusonite structure, space group $I2/a$), complete solid solutions were prepared. In these solid solutions, the unit cell volume decreases as the Ta content increases. The subtle interaction evident between the *Ln*O_8 and *B*O_6 sublattices in the fergusonite-type oxides was not observed in the related pyrochlore oxides. A combined synchrotron X-ray and neutron powder diffraction study of the series Ho$(Nb_{1-x}Ta_x)O_4$ was used to determine accurate atomic positions of the anions, and hence, bond lengths. This revealed a change in the (Nb/Ta)-O bond lengths, reflective of the difference in the valence orbitals of Nb(4*d*) and Ta(5*d*). Examination of the partial density of states demonstrates differences in the electronics between Nb and Ta, leading to a difference in the bandgap. This study highlights the importance of the long *B*-O contacts in the fergusonite structures, and its potential impact on the $I2/a$ to $I4_1/a$ phase transition.

Introduction

The ABO_4 ternary oxides are of considerable interest due to their potential application as photocatalysts, nuclear waste storage materials, and as high-temperature ionic conductors for solid-oxide fuel cells.[1-3] These oxides have been extensively studied due to the flexibility in their crystal lattice that can accommodate combinations of cations in various oxidation states forming a variety of structures.[4-6] In particular, oxides with a $CaWO_4$ scheelite-type structure are of great interest from both a theoretical and technological point of view, given their exotic magnetic structures and practical application in optoelectronic devices.[7-12] The tetragonal scheelite structure (space group $I4_1/a$, #88) consists of AO_8 dodecahedra and unlinked BO_4 tetrahedra (see Figure 1a). The scheelite structure has been shown to exhibit spontaneous ferroelastic strain, resulting in properties such as optical absorption in $BiVO_4$ and increased microwave dielectric properties in $La(Nb_{0.7}V_{0.3})O_4$.[13, 14] The fergusonite structure (space group $I2/a$ – an alternate setting of $C2/c$, #15), often described as a monoclinic distortion of the scheelite aristotype,[15] contains similar AO_8 dodecahedra but with distorted edge-sharing BO_6 polyhedra forming B_2O_9 moieties.[16] The two long B-O bonds (~ 2.5 Å) in the BO_6 polyhedra of the $I2/a$ structure, that are absent in the BO_4 tetrahedra of the $I4_1/a$ structure, have been identified as important structural features that potentially impact the ionic conductivity of the material.[17-23] The structure of the fergusonite oxides is influenced by either temperature or pressure, with $LnNbO_4$ (Ln = lanthanoid, La-Lu) undergoing a ferroelastic phase transition from $I2/a$ to $I4_1/a$ at high temperatures, and undergoing a reversible phase transition to a second monoclinic form (space group $P2_1/c$, #14) at high pressures.[24-27] A recent high pressure study on fergusonite type $YbNbO_4$ shows a non-reversible monoclinic to triclinic phase transition. The impact of the long B-O bonds on the thermally-induced transition between the fergusonite and scheelite structures has often been overlooked in favor of a ferroelastic explanation. However, a recent study on the phase transition of $NdNbO_4$ and $NdTaO_4$ has shown that the breaking of the long B-O bond may be the driver for the first order nature of the phase transition, with the strength of such bonds impacting the transition temperature.[28]

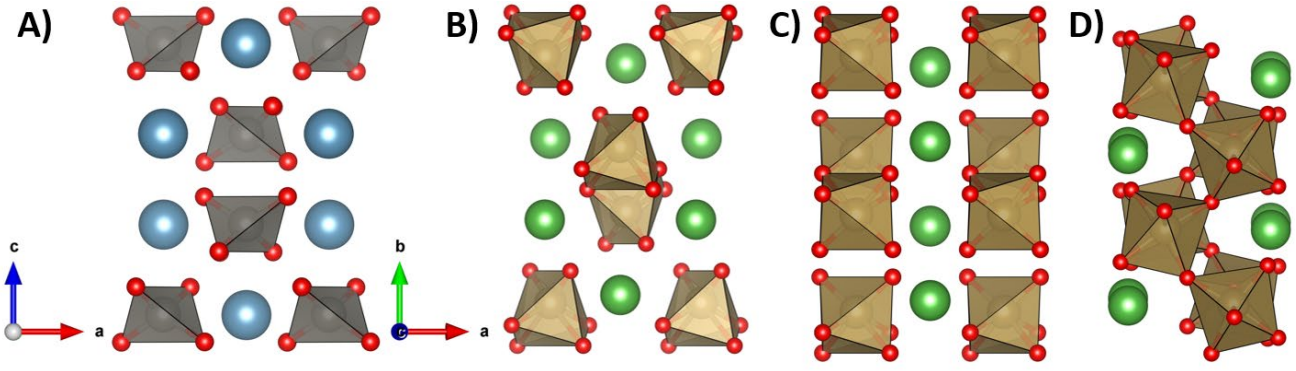

Figure 1: Representations of (A) the tetragonal scheelite structure ($I4_1/a$) (B) the $I2/a$ fergusonite structure, (C) the $P2/c$ $YTaO_4$-type structure, and (D) the $P2_1/c$ $LaTaO_4$-type structure.

Various phase diagrams of the ABO_4 structures have been proposed based on the r_A/r_O and r_B/r_O ionic radii ratios.[4, 5] However, there are numerous exceptions and the precise structure adopted by a particular ABO_4

compound cannot always be predicted based on size arguments alone. Experimental work has found the structures can be sensitive to their synthesis conditions.[16, 29] This is evident in various $LnBO_4$ (*Ln* = La-Lu; *B* = Nb, Ta) structures described in the literature. The $LnNbO_4$ oxides invariably form the monoclinic *I*2/*a* fergusonite structure when prepared using ambient pressure solid state methods, whereas the analogous $LnTaO_4$ oxides prepared under the same conditions form a variety of structures.[30-33] This is remarkable, considering Nb^V and Ta^V are described as displaying near-identical crystal chemistry as a result of their identical ionic radii.[34] Even when they form isostructural oxides, there are significant structural differences between the $LnNbO_4$ and $LnTaO_4$ oxides. In particular, the monoclinic β angle and the atomic position of the cations are significantly different. Similar variances have also been noted in thin film ceramics, such as ~~the~~ changes in structure between $EuNbO_4$ and $EuTaO_4$, and the differences in the luminescent properties of $GdNbO_4$ and $GdTaO_4$.[35, 36]

The differences between the crystal and electronic structure of $LnNbO_4$ and $LnTaO_4$ have a major impact on the observed ferroelastic phase transition, which in turn impacts the working temperature of the material as a thermal barrier coating or a potential solid electrolyte.[36, 37] The temperature of the phase transition from the monoclinic *I*2/*a* to the tetragonal $I4_1/a$ structure in $LnNbO_4$ increases as the ionic radii of the lanthanoid cation decreases, as experimentally determined by Arulnesan *et al.* and Sarin *et al.* using powder X-ray ~~powder~~ diffraction (PXRD).[25, 31] This trend has also been observed in the corresponding tantalates, although the transition occurs at much higher temperatures.[28, 38] Debate exists in the literature as to why, despite the identical ionic radii and similar crystal chemistry of Nb^V and Ta^V, the $LnNbO_4$ and $LnTaO_4$ compounds display such different phase transition temperatures.[15, 38, 39] It has been suggested that the atomic position of Nb^V in the NbO_6 distorted octahedra of the *I*2/*a* structure is closer to the ideal position of Nb^V in the NbO_4 tetrahedra of the $I4_1/a$ structure, hence there is less of an energy barrier to the *I*2/*a* to $I4_1/a$ phase transition in the niobates than in the corresponding tantalates.[40] It has also been suggested that the smaller unit cell of $LnTaO_4$ increases the monoclinic β angle, leading to a higher monoclinic-to-tetragonal phase transition temperature.[28] Recently, Mullens *et al.* [28] demonstrated, using density-functional theory (DFT) calculations, that the electron charge density and Born effective charge (BEC) were different between the two end-members of the $Sm(Nb_{1-x}Ta_x)O_4$ and $Ho(Nb_{1-x}Ta_x)O_4$ series. This suggests the structural differences between the $LnNbO_4$ and $LnTaO_4$ series may be driven by electronic effects.[16]

There are several examples, not restricted to the $Ln(Nb/Ta)O_4$ structure, that demonstrate the subtle differences in crystal chemistry between Nb^V and Ta^V. The isostructural perovskites $LiNbO_3$ and $LiTaO_3$ undergo a high-temperature phase transition at different temperatures ($LiNbO_3$ ~ 1200 °C, $LiTaO_3$ ~ 620 °C) due to the more covalent Nb-O bonds and the tendency of Ta^V to distort away from the center of the ideal octahedral coordination[40]. There are also significant differences in the phase transition behavior of $NaNbO_3$ and $NaTaO_3$, as well as of $AgNbO_3$ and $AgTaO_3$.[41-45] Structural distortions have been noted in other Nb^V- and Ta^V-containing perovskites that have been attributed to the second-order Jahn-Teller distortion of the d^0 Nb^V and Ta^V cations in their octahedral environment.[46] Such distortions can impact the ferroelectric properties of different layered perovskite-type structures, with a higher ferroelectric Curie temperature observed for Nb-

containing Aurivillius and tungsten-bronze structures than the corresponding Ta-containing compounds.[47, 48] It is clear that, despite having the same ionic radii, the electronic properties of Nb^V and Ta^V are sufficiently different, and this can lead to differences in their structural and physical properties.

The current work is concerned with understanding the chemical, electronic and structural differences in the *Ln*(Nb/Ta)O_4 oxides. To complement and extend the earlier work of Arulnesan *et al.*[31] on the *Ln*NbO_4 series, this study first describes the structures of the different polymorphs of the *Ln*TaO_4 oxides using synchrotron X-ray diffraction (SXRD). This is followed by a study of the impact of the progressive replacement of Nb^V by Ta^V across several *Ln*($Nb_{1-x}Ta_x$)O_4 series to identify how each structure changes. A combination of SXRD and NPD was employed to determine the long-range average structure of the Ho($Nb_{1-x}Ta_x$)O_4 solid-solution series, with X-rays and neutrons being more sensitive to the cation and anion sublattices respectively. This revealed subtle changes in the polyhedra volume, bond lengths, and atomic positions between Nb^V and Ta^V compounds. Finally, the partial density of states of various *Ln*(Nb/Ta)O_4 compounds were examined using density functional theory to determine the differences in their electronic structure.

Experimental

Samples with the composition *Ln*TaO_4 (*Ln* = La-Lu, excluding Ce, Pm) were prepared using a conventional solid-state synthesis route. Appropriate stoichiometric mixtures of high purity (99.9-99.99 wt %) Ln_2O_3, Pr_6O_{11}, Tb_4O_7, and Ta_2O_5 (Aithaca), sufficient to prepare 2 g of each sample, were dried at 1000 °C for 15 hours to remove adsorbed water and CO_2. The metal oxides were first weighed and then an acetone slurry of these was finely mixed by hand in an agate mortar. The dried powder was placed in an alumina crucible and heated at 1000 °C for 24 hours. After hand-mixing again, the samples were pressed into rods using a hydrostatic press at 200 bar for 10 mins. The rods were then heated in air at 1200 °C for 24 hours and 1400 °C for 48 hours, with intermittent grinding and repressing.

Samples with composition *Ln*($Nb_{1-x}Ta_x$)O_4 (*Ln* = Pr, Nd, Gd, Tb, Dy, Yb, and Lu; x = 0.0-1.0 with Δx = 0.2. *Ln* = Sm, Ho; x = 0.0-1.0 with Δx = 0.1) were prepared using the same solid-state synthesis route described above. Appropriate stoichiometric mixtures of Ln_2O_3, Pr_6O_{11}, Tb_4O_7, Nb_2O_5 and Ta_2O_5 (Aithaca), sufficient to prepare 2 g of each sample, or in the case of the Ho-series 8 g, were dried at 1000 °C for 15 hours to remove adsorbed water and CO_2. The metal oxides were weighed and finely mixed by hand in an agate mortar using acetone as a milling agent, before being heated at 1000 °C, 1200 °C and 1400 °C, with intermittent grinding and repressing.

Polycrystalline samples of the pyrochlore series Ln_2($Zr_{2-x}Sn_x$)O_7 (*Ln* = La, Pr, Sm; x = 0.0-2.0 with Δx = 0.4) were also synthesized using a conventional solid-state synthesis route. These *Ln* cations were chosen such that the synthesized samples would form the pyrochlore structure (space group $Fd\bar{3}m$, #227) across the entire series.[49] Appropriate stoichiometric mixtures of Ln_2O_3, ZrO_2 (99% Sigma-Aldrich), and SnO_2 (99.99% Sigma-Aldrich), sufficient to prepare 2 g of each sample, were dried at 1000 °C for 15 hours to remove adsorbed water and CO_2. The samples were ground in a mortar as above, pressed into rods and heated at 1000 °C for 24

hours and 1650 °C for 48 hours with intermittent grinding and re-pressing. The samples were cooled at a rate of 0.1 °C min^{-1} to 1000 °C to ensure high crystallinity of the product.[50, 51]

Synchrotron X-ray powder diffraction (SXRD) data were collected for the $LnBO_4$ series over an angular range $5° < 2\theta < 85°$, at 16 or 18 keV, the precise wavelength being determined by structural refinement of a NIST SRM660b LaB_6 standard, on the powder diffractometer beamline BL-10 of the Australian Synchrotron.[52] The samples were each housed in 0.2 mm diameter glass capillaries that were rotated during the measurements to minimize preferred orientation effects. Neutron powder diffraction (NPD) measurements were performed on Echidna, the high-resolution powder diffractometer at the Open Pool Australian Lightwater (OPAL) reactor, operated by the Australian Nuclear Science and Technology Organisation (ANSTO).[53] Powder samples of the Ho-containing oxides were loaded into 9 mm diameter vanadium cans, with data collected over the range $5° < 2\theta < 162°$ with a step size of 0.05° at a wavelength of 1.6215 Å.

Structures were refined using the Rietveld method as implemented in the program TOPAS 5 using either the SXRD or a combined SXRD and NPD dataset.[54] The peak shapes were modelled using a pseudo-Voigt function, and the background of each pattern was estimated using a 12^{th}-order Chebyshev polynomial. The scale factor, lattice parameters, atomic positions, and displacements parameters (ADPs) were refined simultaneously with the peak profile parameters. ADPs were taken to be isotropic and equal across each Wyckoff position (regardless of cation mixing). For the $Ln(Nb_{1-x}Ta_x)O_4$ data, the Stephens phenomenological model of anisotropic peak broadening was utilized. In the final refinement cycle, the parameters were fully relaxed with all free parameters refined. The crystal structures were drawn using VESTA.[55]

Computational results were obtained using DFT calculations[56, 57] as implemented in the Vienna *ab initio* simulation package (VASP) version 5.4.4, based on projector augmented wave (PAW) method.[58] In order to account for the exchange-correlation contribution, the generalized gradient approximation (GGA) functional Perdew-Burke-Ernzerhof (PBE)[59] and its different flavor PBEsol[60] were used. A typical valence of 3 was used for the *Ln* atoms where the 4*f* electrons were treated as core electrons. The following electronic configurations were used: Pr: $5s^2 5p^6 5d^1 6s^2$, Gd: $5p^6 5d^1 6s^2$, Ho: $5p^6 5d^1 6s^2$, Yb: $5p^6 5d^1 6s^2$, Ta:$5p^6 6d^1 5d^4$, Nb: $4p^6 5s^1 4d^4$, O: $2s^2 2p^4$. The cut-off value for the planewave basis set was set to 800 eV for all crystal structures. Brillouin zone sampling of these crystals was considered through the Monkhorst-Pack (MP)[61] grids where the following Γ-centered *k*-grids were employed: 9 × 5 × 10 for $GdNbO_4$ and $GdTaO_4$, 9 × 4 × 10 for $PrNbO_4$, 7 × 9 × 7 for $PrTaO_4$, 10 × 5 × 10 for $YbNbO_4$, and 10 × 9 × 10 for $YbTaO_4$. The algorithm of Broyden-Fletcher-Goldfarb-Shanno (BFGS)[62] was used for the structural optimization. The criteria for convergence were set as: 0.001 eV $Å^{-1}$ for force minimization and 1×10^{-8} eV for energy minimization. The unit cell size and shape were allowed to vary under the symmetry constraints of the corresponding space groups.

Results and Discussion

(i) *Synchrotron X-Ray Diffraction Analysis of $LnTaO_4$ (Ln = La-Lu, excluding Ce, Pm)*

The synthesis of crystalline single-phase samples of the lanthanoid orthotantalates, $LnTaO_4$, was achieved using solid state reactions with a maximum annealing temperature of 1400 °C. Each sample was heated at 1400 °C for 48 hours to ensure no unreacted Ln_2O_3 or Ta_2O_5 remained. As reported by Brixner *et al.* and Haugsrud *et al.*, the $LnTaO_4$ oxides crystallize into different structures depending on the size of the *Ln* cation and the synthetic conditions.[37, 63]

For $LnTaO_4$ (*Ln* = La, Pr), the SXRD patterns were successfully indexed to the $P2_1/c$ structure, with lattice parameters in good agreement with previous literature.[63-65] No evidence of other high-temperature phases, such as the weberite-type Ln_3TaO_7 (space group *Cmcm*, #63), defect perovskite $Ln_{1/3}TaO_3$ (space group *P4/mmm*, #123), or the layered oxide $LnTa_3O_9$ (space group *Pnma*, #62) was observed.[66-68] For *Ln* = Nb-Tb, the patterns were indexed to the *I*2/*a* structure. For *Ln* = Dy-Lu, the *P*2/*c* structure was appropriate. Representative Rietveld refinements are shown in Figure 2, with the full results of these refinements summarized in the Electronic Supplementary information (ESI).

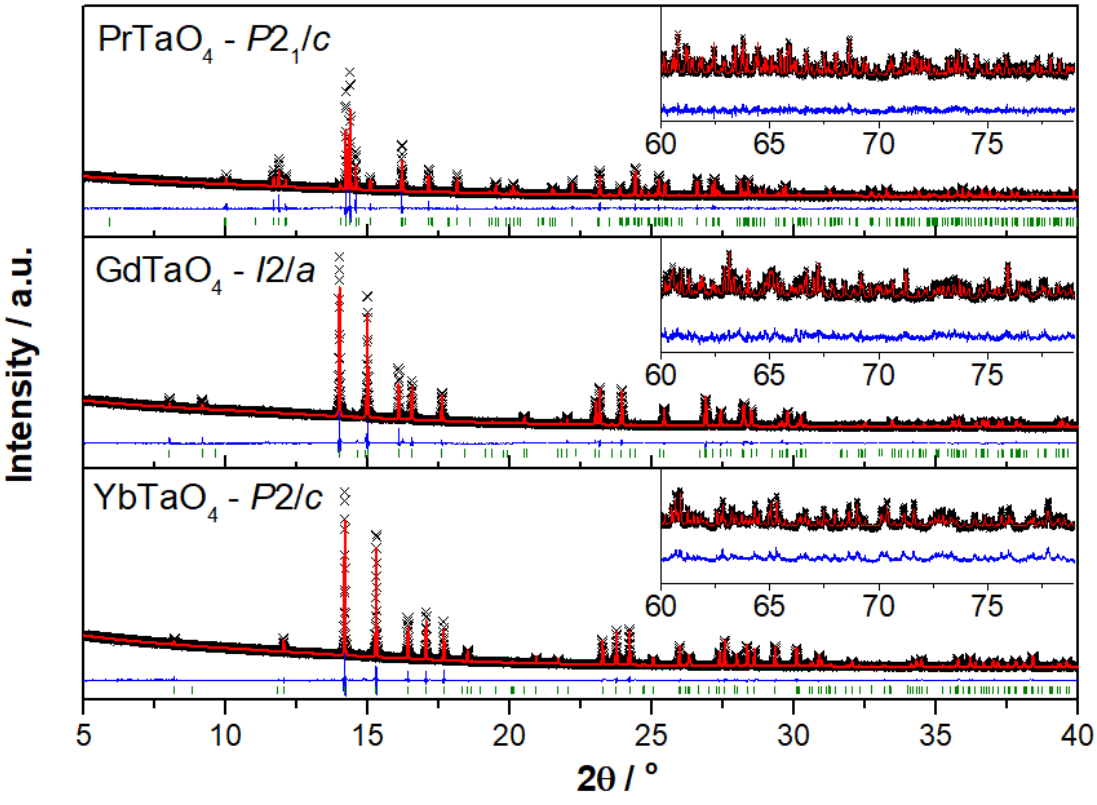

Figure 2: Representative Rietveld plots for $PrTaO_4$ (Top) fitted in space group $P2_1/c$, $GdTaO_4$ (Middle) fitted in *I*2/*a*, and $YbTaO_4$ (Bottom) fitted in *P*2/*c*. The black crosses are the observed SXRD data, collected at 0.77461(2) Å, the solid red line is the calculated profile, and the solid blue line is the difference between the observed and calculated intensities. The insets highlight the quality of the data and fits at high angles. The vertical tick marks show the positions of the space group allowed Bragg reflections.

The *Ln*TaO_4 oxides crystallize with different monoclinic structures depending on the lanthanoid cation and the synthesis conditions.[63] For example, Brixner *et al.* demonstrated that *Ln*TaO_4 (*Ln* = Sm-Lu) could crystallize in either the *P*2/*c* or *I*2/*a* space group dependent on whether a 50% wt $LiSO_4$ or LiCl flux was used.[63] Other workers have reported similar effects.[69-71] In the current work, samples of *Ln*TaO_4 were heated, without a flux, to different temperatures to determine the temperature at which the *P*2/*c* or *I*2/*a* phase could be formed. $TbTaO_4$ adopted the *P*2/*c* structure when annealed at 1350 °C and the *I*2/*a* structure when annealed at 1400 °C. Similarly, for $DyTaO_4$ and $HoTaO_4$, the *P*2/*c* structure was recovered after heating at 1400 °C and the *I*2/*a* recovered when the temperature was increased to 1450 °C. Attempts to recover $GdTaO_4$ in the *P*2/*c* structure through lowering the final annealing temperature were unsuccessful. Efforts to recover the *I*2/*a* structure of $ErTaO_4$ were partially successful. After annealing at 1550 °C, the PXRD pattern for $ErTaO_4$ measured using a laboratory diffractometer with Cu radiation could be successfully fit using the *I*2/*a* structural model. However, subsequent SXRD data showed the sample contained a mixture of the *I*2/*a* + *P*2/*c* polymorphs (see the ESI). Including the *P*2/*c* phase in the refinement model improved the fit from R_{wp} = 11.5%, R_p = 6.06%, χ^2 = 77.6 (*I*2/*a* model) to R_{wp} = 4.31%, R_p = 2.86%, χ^2 = 10.8 (*I*2/*a* + *P*2/*c* model). This suggests that a higher annealing temperature could yield the pure *I*2/*a*. Wang *et al.* previously prepared the *I*2/*a* polymorph of $ErTaO_4$ by annealing at 1700 °C.[72]

Interestingly, there appears to be a correlation between the preferred (*P*2/*c* or *I*2/*a*) structure, the highest heating temperature, and the temperature of the reversible *I*2/*a* to *I*4_1/*a* phase transition. The *I*2/*a* to *I*4_1/*a* phase transition for $TbTaO_4$ and $HoTaO_4$ is (1410 ± 15) °C, which is around the temperatures used in this work to transform the *P*2/*c* polymorph to the *I*2/a polymorph. Limiting the maximum temperature to below the *I*2/*a* to *I*4_1/*a* transition temperature invariably resulted in recovery of the *P*2/*c* polymorph, whereas heating above the *I*2/*a* to *I*4_1/*a* transition temperature yielded the *I*2/*a* polymorph. In general, synthesis of the samples containing the larger *Ln* cations (Sm-Gd) at 1400 °C resulted in isolation of phase pure samples of the *I*2/*a* polymorph. This is consistent with the observation of the *I*2/*a* to *I*4_1/*a* transition temperature increasing as the size of the *Ln* cation decreases. It is postulated that for *Ln*TaO_4 (*Ln* = Tb-Er), the *P*2/*c* structure is kinetically favored, whereas the *I*2/*a* structured polymorph is the thermodynamic favored phase that can be recovered by passing through the high-temperature *I*4_1/*a* phase. Gagarin *et al.* reported that members of the *Ln*TaO_4 series undergo a high-temperature modification that may change the space group of the final cooled product, however they failed to provide any detail as to what influenced the stability of the final product. A similar observation was made by Stubičan *et al.*, however to date the only *in-situ* diffraction studies reported describe the reversible *I*2/*a* to *I*4_1/*a* phase transition and not the irreversible *P*2/*c* to *I*2/*a* transformation.[38]

The unit cell parameters and unit cell volume of the *Ln*TaO_4 (*Ln* = Nd-Lu) series are plotted in Figure 3 and Figure 4 respectively. In these figures, the values for the two *Ln*TaO_4 oxides with *Ln* = La and Pr were excluded as their *P*2_1/*c* structure is sufficiently different from the *P*2/*c* and *I*2/*a* structures. For the *P*2/*c* and *I*2/*a* structure types, the unit cell parameters and volumes increase linearly as the ionic radii of the lanthanoid cation increases. The absence of any discernible deviation from linearity in the various unit cell parameters also shows

that Tb is present in its trivalent state despite Tb_4O_7 being used as a precursor. The atomic coordinates of the cations refined in this work are in excellent agreement with values reported previously where these are available. For both structural types, the monoclinic β angle appears to be only weakly dependent on the size of the *Ln* cations, with a larger monoclinic β angle observed in the *P*2/*c* polymorphs, as shown in Figure 4.

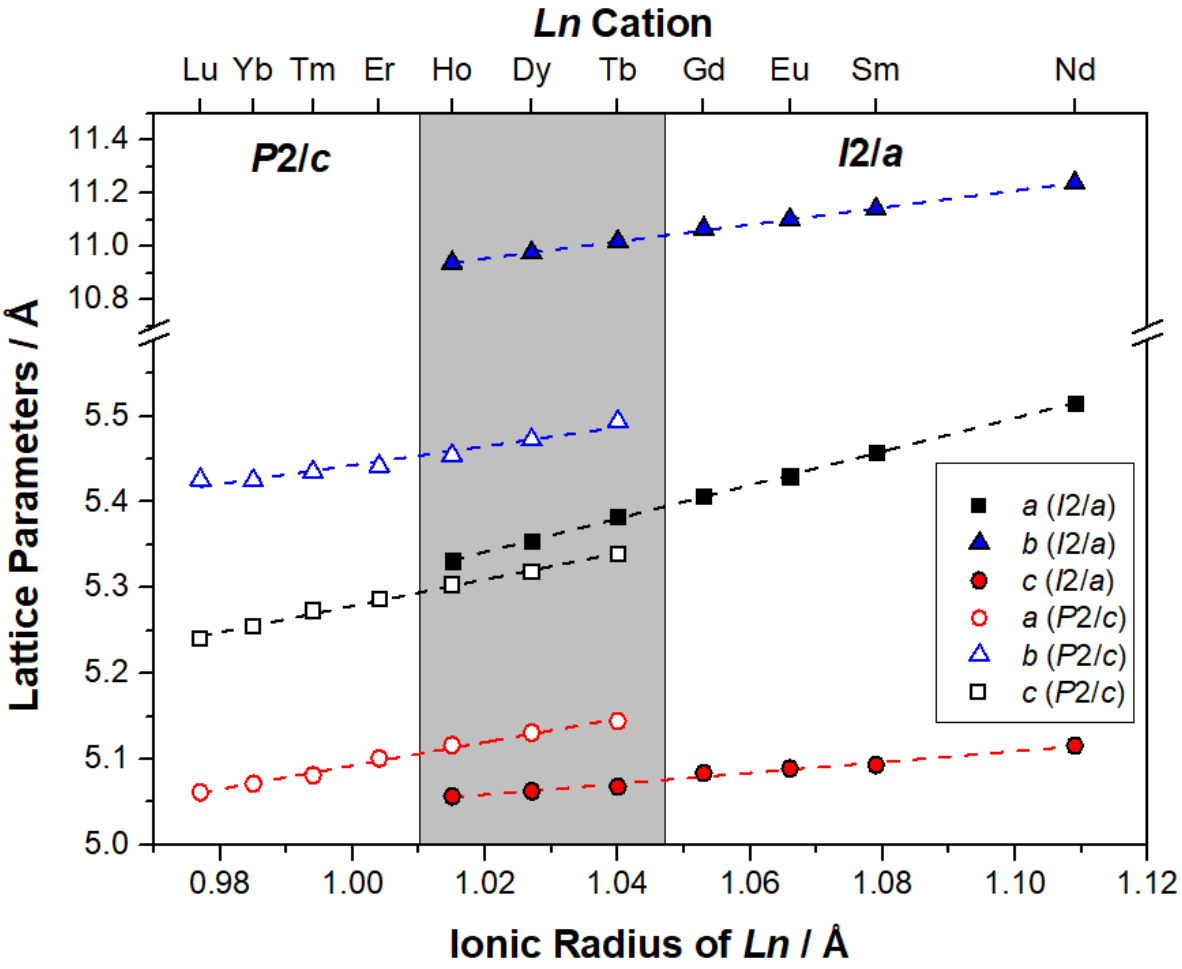

Figure 3: Composition dependence of the room temperature unit cell parameters of the *Ln*TaO_4 series. Where not apparent, the errors are smaller than the symbols. For the samples inside the grey area (*Ln* = Ho, Dy, and Tb) single phase samples of both polymorphs were recovered and studied. The dashed linear lines have been drawn to guide the eyes.

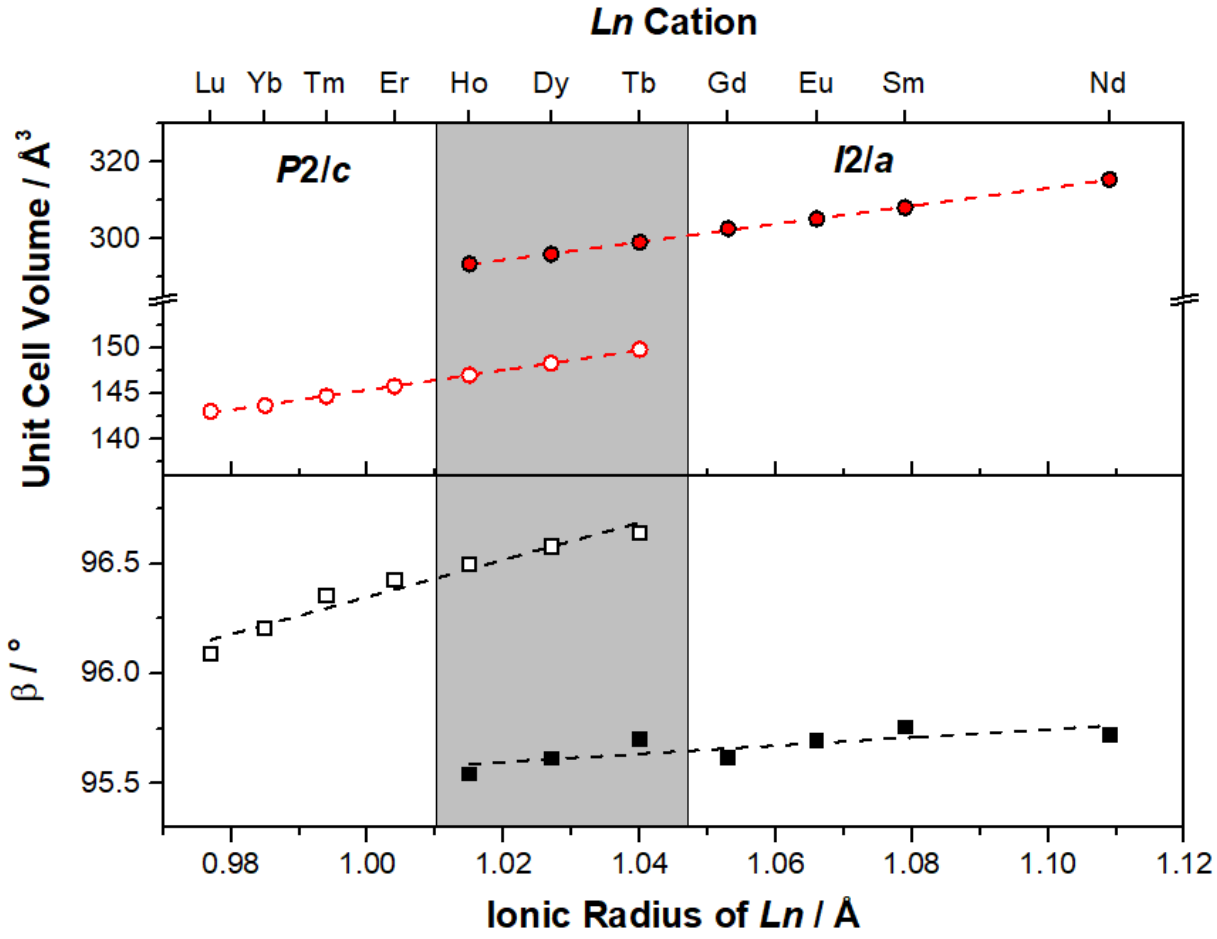

Figure 4: Composition dependence of the room temperature unit cell volume and monoclinic β angle of the LnTaO$_4$ series. Where not apparent, the errors are smaller than the symbols. For the samples inside the grey area (Ln = Ho, Dy, and Tb) single phase samples of both polymorphs were recovered and studied. Dashed linear lines have been drawn to guide the eyes.

Despite the presence of very heavy cations in the LnTaO$_4$ oxides, the extended d-range afforded by the use of relatively high energy X-rays (d_{min} < 0.59 Å) resulted in relatively accurate and precise values for the anion atomic coordinates, and hence the Ln-O and Ta-O distances. This was performed due to the limited number of neutron diffraction studies of these oxides.[73] Some authors have described the Nb and Ta cations in the $I2/a$ structure as having a four-coordinate tetrahedral arrangement. However, both the Nb^V and Ta^V cations are considered too large for a tetrahedra geometry, and are mostly encountered as octahedrally coordinated in oxides such as the perovskites Na(Nb/Ta)O$_3$, La$_{1/3}$(Nb/Ta)O$_3$ and in layered oxides such as the Aurivillius phases SrBi$_2$(Nb/Ta)$_2$O$_9$.[45, 47, 67] The bond valence sum analysis of the $I2/a$ structured oxides revealed the contribution of two additional long bonds (Ta-O$_L$), showing that the Ta cations are better described as having a six-coordinate distorted octahedral geometry. The bond valence sum (BVS) for Ta was calculated as S_{ij} = exp[($R_0 - R_{ij}$)/B], where R_{ij} is the observed bond length, R_0 is a tabulated constant for the (ideal) bond length, and B is an empirical constant.[74] Inclusion of the longer Ta-O contacts gives a more reasonable value for the

BVS for both the *I*2/*a* and *P*2/*c* structures (S_{ij} = 4.8-5.5 for TaO_6 compared to 4.2-4.8 for TaO_4). The BVS of the LnO_8 polyhedra also displayed unexceptional values across both the *P*2/*c* and *I*2/*a* structures. A full list of the BVSs are given in Table S1 of the supporting information.

Figure 5 illustrates the changes in the *Ln*-O and Ta-O bond lengths for both structural types, as well as the changes in their polyhedra volume. Across each of the *P*2/*c* and *I*2/*a* series, the average *Ln*-O bond distances and the LnO_8 polyhedra volume increase as the size of the *Ln* cation increases. As expected for each structural type, the average Ta-O bond distances remain essentially independent of the size of the *Ln* cation. The average Ta-O bond length and TaO_6 polyhedra volume appear to be larger in the *I*2/*a* structure compared to the *P*2/*c* polymorph, potentially due to the overall smaller unit cell volume of the *P*2/*c* structure.

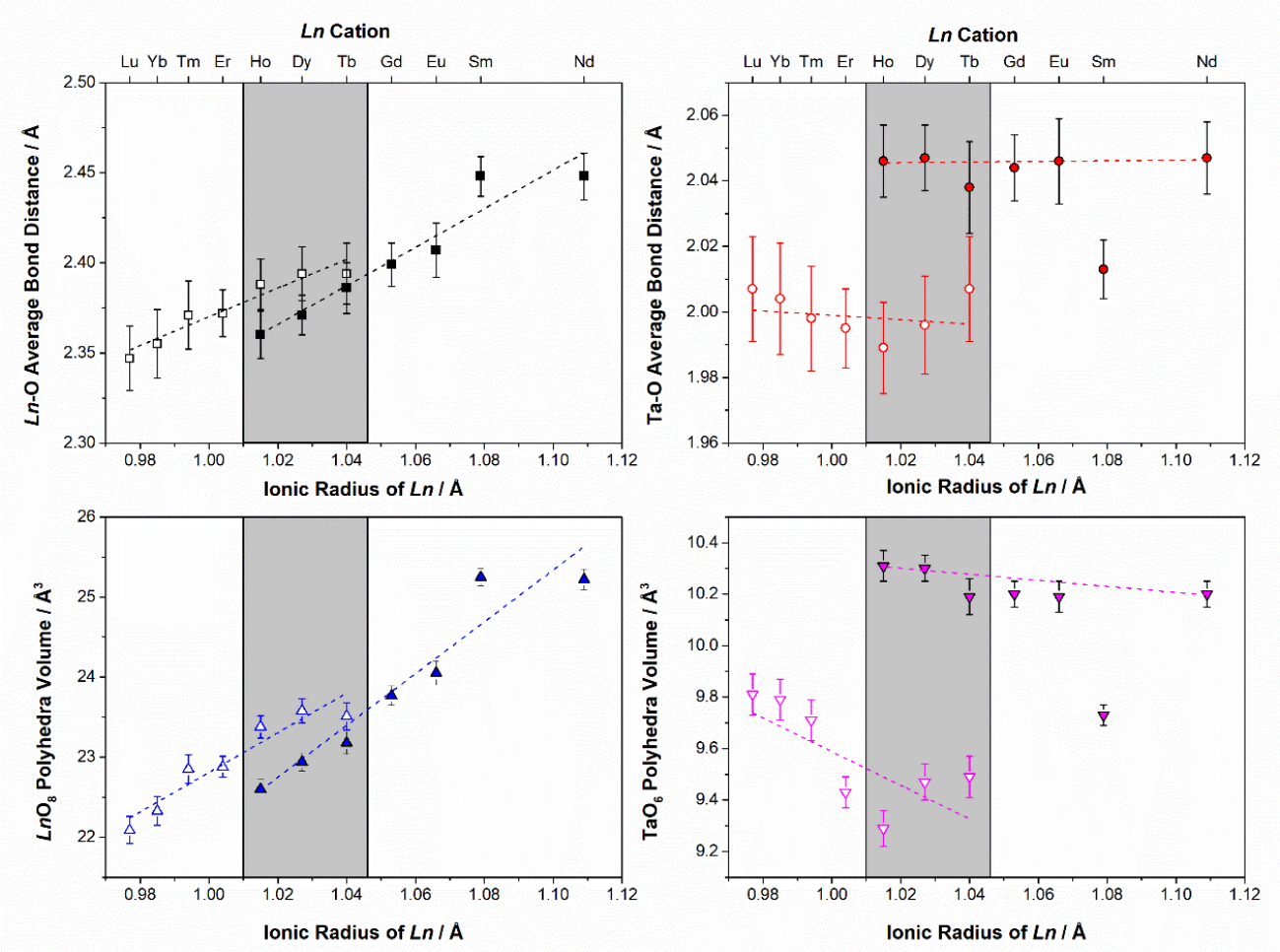

Figure 5: Composition dependence of the *Ln*-O and Ta-O average bond lengths (Top) and the volume of the LnO_8 and TaO_6 polyhedra (Bottom). The open symbols are for the structures in space group *P*2/*c* and the closed symbols are for structures in *I*2/*a*. Single phase samples of both polymorphs were studied for *Ln* = Ho, Dy, and Tb, and are indicated by the shaded region

Figure 6 illustrates the compositional dependence of the individual bond distances. One interesting observation is the reduction in the long *Ln*–O bond length (denoted as *Ln*-$O(2)_L$ in the figure) in the *P*2/*c* series with increasing *Ln* radii. This is accompanied by an increase in the other *Ln*-O bond distances. This difference

may partially explain why some LnTaO$_4$ structures cannot be synthesized with the $I2/a$ fergusonite-type structure. This may be analogous to the changes in the structural types exhibited by the Ln_2O_3 sesquioxides, where the structure is dependent on the choice of Ln cation.[75] Neutron diffraction could be used to increase the accuracy of the refined structures, especially the anion positions, although it is unlikely to change the observed trends. We further note that this is not trivial for materials containing strongly absorbing elements such as Sm, Eu and Gd.

In summary, the SXRD data demonstrates the synthesis of the LnTaO$_4$ oxides with the structures described as one of three monoclinic space groups: $P2_1/c$, $I2/a$, or $P2/c$. The observed structure is determined by the size of the Ln cation and the heating conditions, with the largest Ln cations crystallizing in either the $P2_1/c$ or $I2/a$ structure, and the smaller Ln cations crystallizing in the $P2/c$ structure. Furthermore, for some Ln cations (Ln = Tb, Dy, Ho), changing the final heating temperature allowed both the $P2/c$ or $I2/a$ polymorphs to be recovered. BVS analysis indicated that Ta^V is six-coordinate in these structures, with four short bonds and two longer bonds. The Ta-O bond lengths are approximately constant across the LnTaO$_4$ series, whilst the Ln-O bond lengths increase as the size of the Ln cation increases.

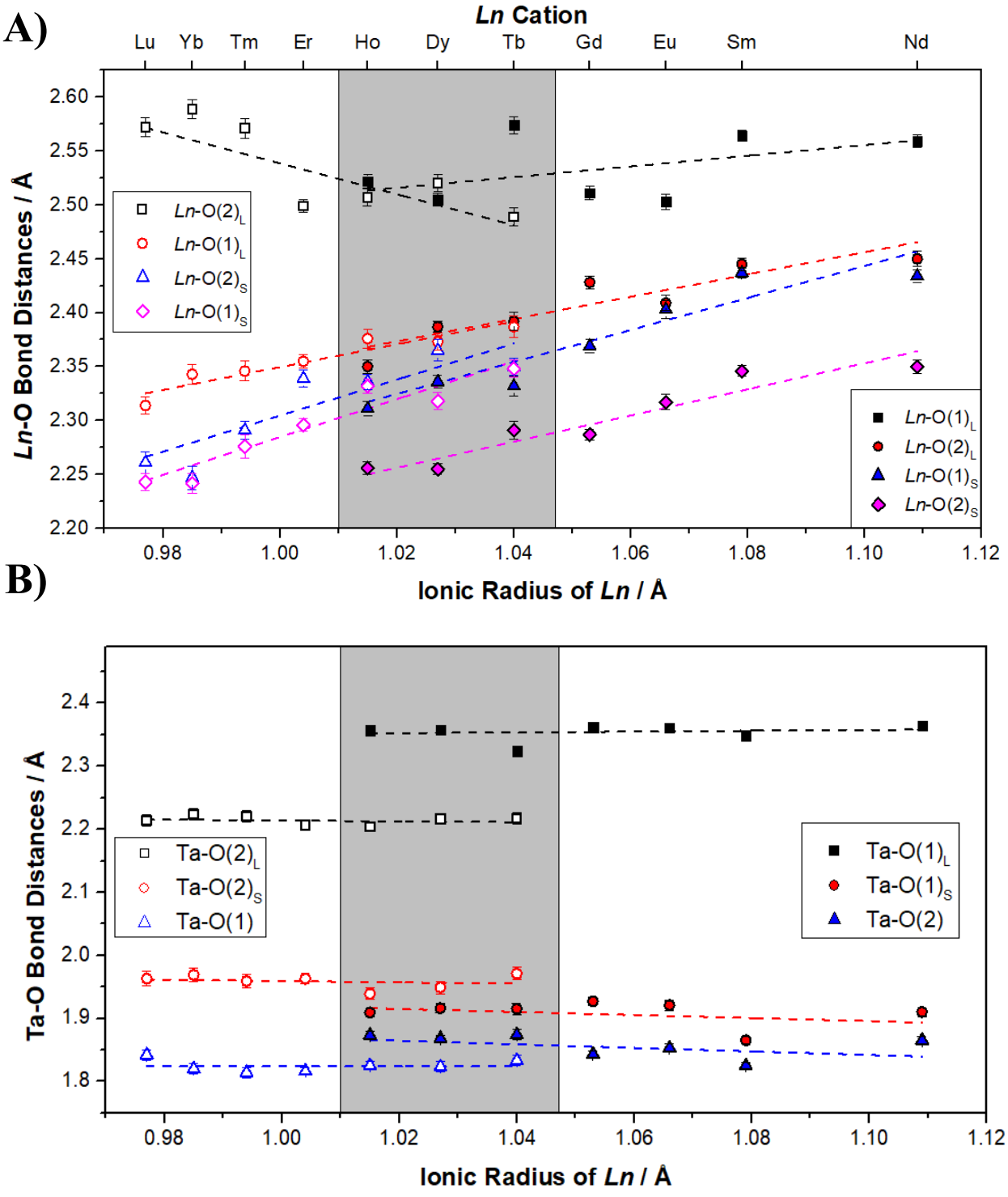

Figure 6: Composition dependence of the *Ln*-O (Top) and Ta-O (Bottom) bond lengths in the *P*2/*c* (Left) and *I*2/*a* (Right) structured oxides in the *Ln*TaO_4 series. The "L" and "S" subscripts signify the "long" and "short" bonds respectively. For the samples inside the grey area (*Ln* = Ho, Dy, and Tb) single phase samples of both polymorphs were recovered and studied. The open symbols are for the structures in space group *P*2/*c* and the closed symbols are for structures in *I*2/*a*.

(ii) *Impact of Nb/Ta Doping in $Ln(Nb_{1-x}Ta_x)O_4$ (Ln = Pr, Nd, Sm, Gd, Tb, Dy, Ho, Yb and Lu)*

Several mixed Nb/Ta oxides of the type $Ln(Nb_{1-x}Ta_x)O_4$ were prepared using solid state reaction methods. The *Ln* cations were selected such that three composition-dependent structural phases could be observed in the different solid-solution series with a final annealing temperature of 1400 °C: *I*2/*a* to $P2_1/c$ (*Ln* = Pr), *I*2/*a* to *I*2/*a* (*Ln* = Nd, Sm, Gd, Tb), and *I*2/*a* to *P*2/*c* (*Ln* = Dy, Ho, Yb, Lu). Rietveld refinements showed that the $LnNbO_4$ structures (x = 0.0) were all described by the monoclinic space group *I*2/*a*, as previously reported by Arulnesan *et al.* and Rooksby *et al.*[31, 65] The behavior observed as Ta was substituted for Nb (increasing x) across each series was dependent on the size of the *Ln* ion, as illustrated in Figure 7. In the $Pr(Nb_{1-x}Ta_x)O_4$ series, the samples with $x \leq 0.8$ had the fergusonite *I*2/*a* structure, whereas $PrTaO_4$ had the $P2_1/c$ structure. This suggests that the solid-solution series changed very abruptly from *I*2/*a* to $P2_1/c$. With the intermediate-sized lanthanoids (*Ln* = Nd-Dy), the structures were in the *I*2/*a* space group at all doping levels. For the smaller lanthanoids (*Ln* = Ho-Lu), the structures of the samples with $x \leq 0.6$ were refined in the space group *I*2/*a*. At higher levels of Ta ($x \geq 0.8$), either both the *P*2/*c* + *I*2/*a* phases co-existed or the sample was single phase in *P*2/*c*. As opposed to the *I*2/*a* to $P2_1/c$ transition observed in $Pr(Nb_{1-x}Ta_x)O_4$, the *I*2/*a* to *P*2/*c* phase transition appears to be more gradual with a two-phase region observed over a range of compositions. The miscibility gap between the *P*2/*c* and *I*2/*a* structures has been noted previously and can be eliminated by heating at higher temperatures.[16] The BVS of each series were also calculated and these calculations supported the hypothesis that the Nb^V and Ta^V remained in a six-coordinate distorted octahedra.

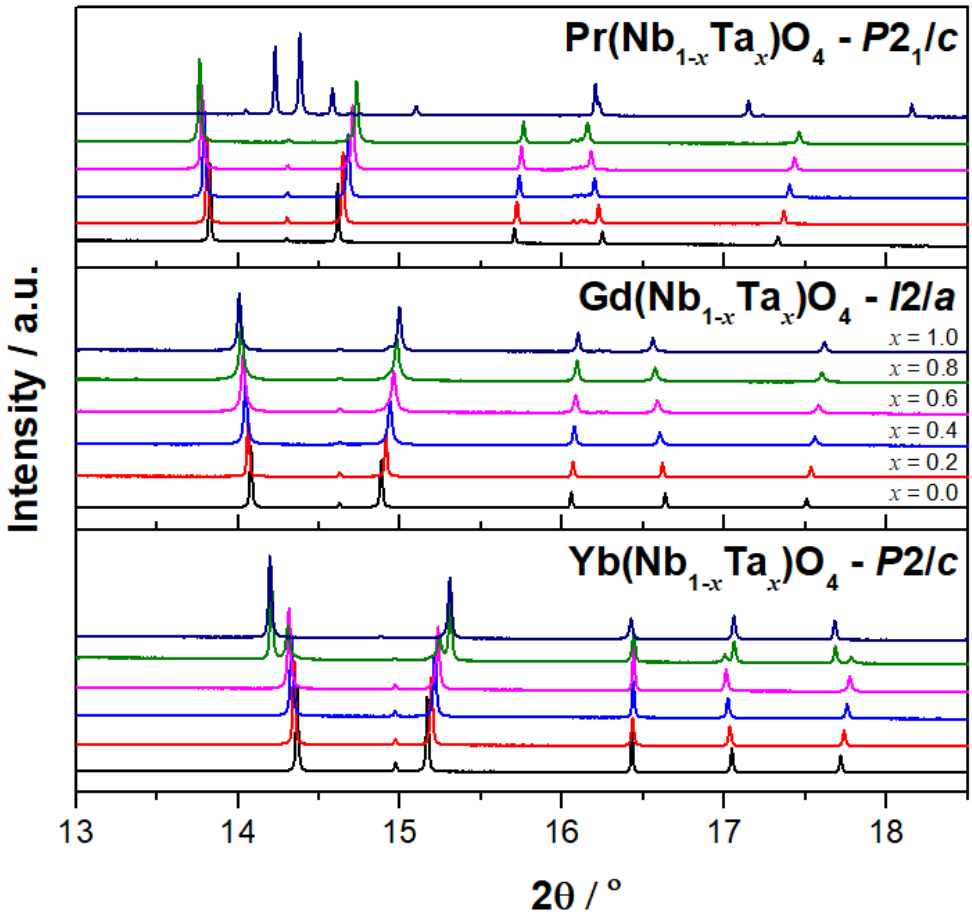

Figure 7: Portions of the SXRD patterns of the three series $Ln(Nb_{1-x}Ta_x)O_4$ (*Ln* = Pr, Gd, Yb). Samples were prepared with x = 0, 0.2, 0.4, 0.6, 0.8 and 1.0. In all cases, the pure Nb oxides (x = 0.0) have the *I*2/*a* structure. The structures of PrTaO4, GdTaO4, and $YbTaO_4$ are described by space groups $P2_1/c$, *I*2/*a*, and *P*2/*c* respectively.

Nb and Ta are often thought to exhibit near-identical crystal chemistry based on the identical value of the ionic radii of Nb^V and Ta^V reported by Shannon.[34] This is despite Ta^V having a 5*d* valence shell compared to the 4*d* shell of Nb^V, as the size of Ta^V is influenced by the lanthanoid contraction. Whittaker *et al.* contrarily concluded that Ta^V is slightly smaller than Nb^V.[76] This conclusion is supported by several examples of oxides where the niobate is larger than the isostructural tantalate, as was observed in our recent studies of $Sm(Nb_{1-x}Ta_x)O_4$ and $Ho(Nb_{1-x}Ta_x)O_4$.[16, 77] Figure 8 compares the normalized unit cell volumes in the $Ln(Nb_{1-x}Ta_x)O_4$ oxides that display the *I*2/*a* structure. In each case the volume of the corresponding niobate (*i.e.*, $LnNbO_4$ where x = 0.0) is taken as unity. All members of each series were heated to the same final temperature, apart from $DyTaO_4$ and $HoTaO_4$ that were heated to 1450 °C. Two features of Figure 8 are remarkable. The first is that across the $Ln(Nb_{1-x}Ta_x)O_4$ series, the tantalate is consistently smaller than the niobate. The second is that the size of the lanthanoid cation appears to play a role in the contraction of the unit cell volume. This is illustrated at x = 1.0 in Figure 8, which shows that $NdTaO_4$ is 0.39% smaller than the isostructural $NdNbO_4$. Conversely, $HoTaO_4$ is only 0.14% smaller than $HoNbO_4$. This implies that the effective ionic radius of Nb^V and Ta^V is dependent on the bonding environment.

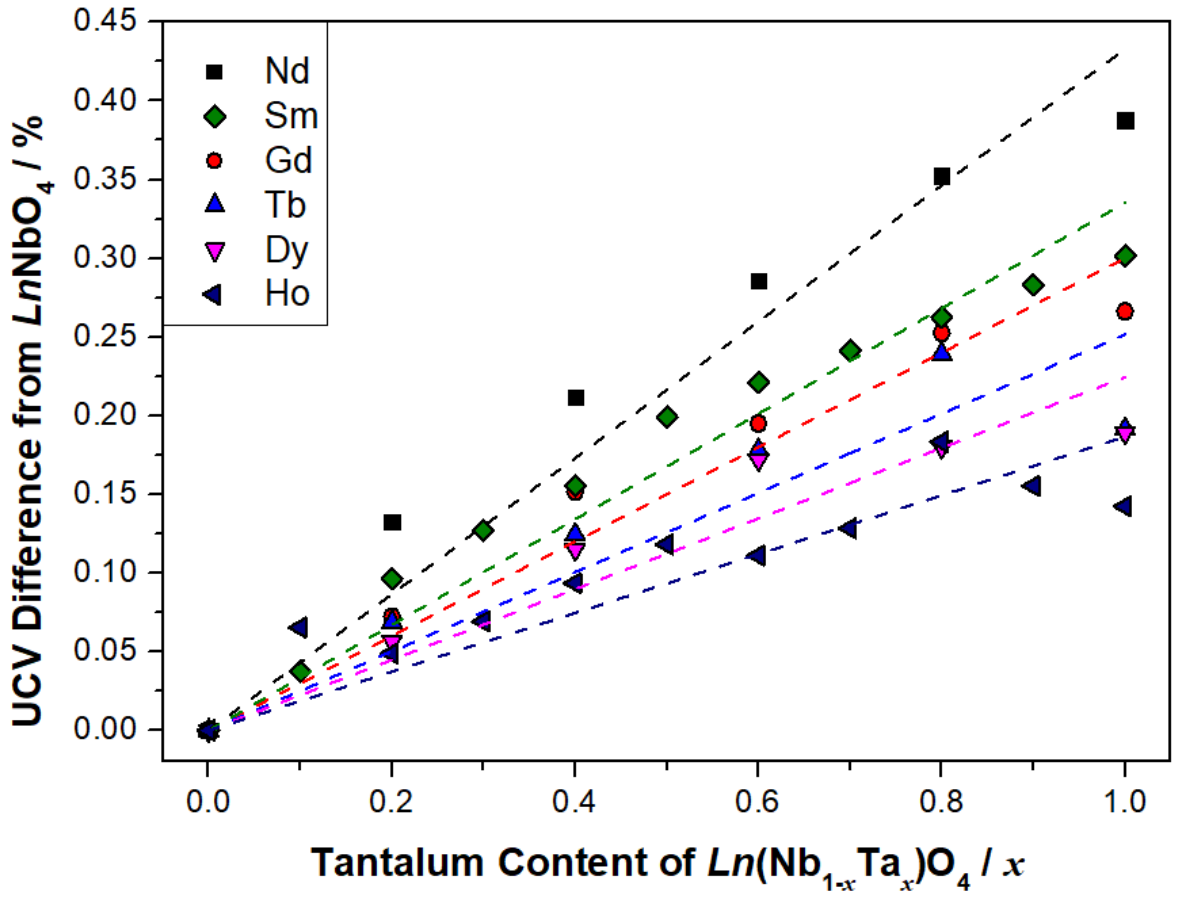

Figure 8: Composition dependence of the normalized unit cell volumes (UCV) for the *I*2/*a* polymorphs of *Ln*($Nb_{1-x}Ta_x$)O_4 oxides. The values are normalized to the values of the corresponding *Ln*NbO_4 structure. The linear fits for each *Ln* series are shown as dashed lines.

To establish if this phenomenon is unique to the fergusonite oxides, three mixed Zr (ionic radius of Zr^{4+} = 0.72 Å) and Sn^{4+} (0.69 Å) pyrochlore series were also studied. Pyrochlores were chosen as they are similarly made up of weakly-interacting *Ln*O_8 and *B*O_6 polyhedra and can incorporate a wide range of metal cations.[50, 51, 78] Figure 9 shows the comparison of the unit cell volume across each pyrochlore series. For each series, the linear fits have essentially identical gradients. This is ~~as~~ expected if the effective ionic radii of the six-coordinate *B*-site cations (Zr^{4+} and Sn^{4+}) is not impacted by either the *Ln* cation or the co-existence of the second *B*-site cation. The relationship between the gradient of the linear fits of the unit cell volume in the *Ln*($Nb_{1-x}Ta_x$)O_4 oxides and the size of the *Ln* cation is shown in Figure 10. A linear relationship exists between the two, with the larger *Ln* cations exhibiting a larger change in the unit cell volume upon Ta substitution than the smaller *Ln* cations. This figure implies that there is an additional interaction between the *Ln*O_8 polyhedra and the (Nb/Ta)O_6 polyhedra in the *I*2/*a* fergusonites that is not apparent in the pyrochlore series. It seems reasonable to conclude that the choice of *Ln* in the *Ln*($Nb_{1-x}Ta_x$)O_4 oxides influences the effective radii of the Nb^{5+} and/or Ta^{5+} cations in the fergusonite structure.

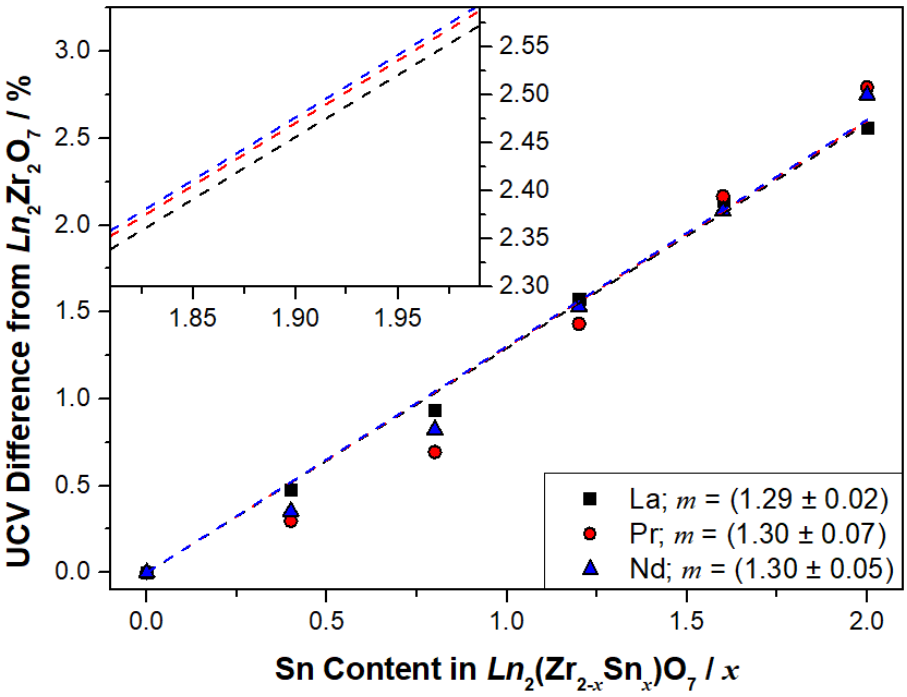

Figure 9: Unit cell volumes of $Ln_2(Zr_{2-x}Sn_x)O_7$ (*Ln* = La, Nd, Sm) pyrochlores plotted as a difference from the original $Ln_2Zr_2O_7$ structure. The linear lines have been added as lines of best fit, with the gradients included in the legend. The inset demonstrates the lack of significant variation between the lines of best fit.

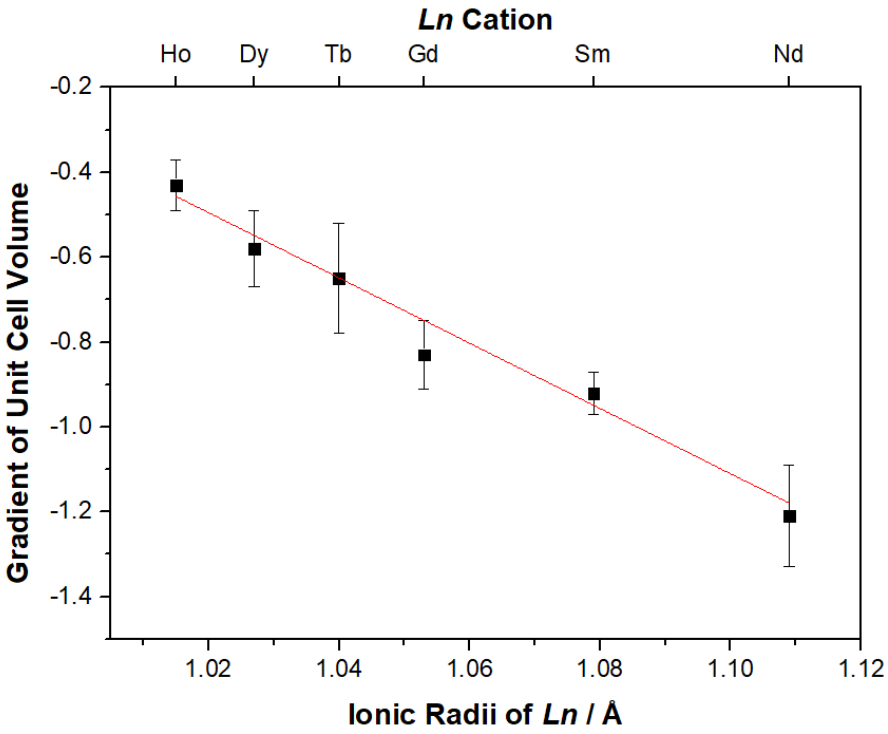

Figure 10: Linear dependence of the gradient change of the unit cell volume between $LnNbO_4$ and $LnTaO_4$ (in the space group $I2/a$) and the size of the *Ln* cation.

(iii) *Ho(Nb$_{1-x}$Ta$_x$)O$_4$ Analysis by Synchrotron X-Ray and Neutron Powder Diffraction*

To further probe the relationship between the two networks of polyhedra in the fergusonite structure, the Ho(Nb$_{1-x}$Ta$_x$)O$_4$ structures were refined against a combined SXRD and NPD dataset. This approach exploits the very precise lattice parameters afforded by the high peak shape resolution in the SXRD measurements and the sensitivity of NPD to the anion positions. The accuracy and precision of the bond distances is dependent on both the lattice parameters and atomic coordinates. Figure 11 displays the average Ho-O and *B*-O bond lengths across the Ho(Nb$_{1-x}$Ta$_x$)O$_4$ series, as well as the HoO$_8$ and *B*O$_6$ polyhedra volumes. The Ho-O average bond length remains essentially constant across the series, whereas the *B*-O average bond length decreases upon substitution of Ta for Nb (increasing *x*). This aligns with our previous observation that the unit cell volume of HoTaO$_4$ is marginally smaller than that of HoNbO$_4$.[16] Both the HoO$_8$ and *B*O$_6$ polyhedra volumes appear to vary across the series, with the HoO$_8$ polyhedra decreasing slightly in volume whilst the *B*O$_6$ polyhedra increase in volume. This supports the hypothesis that interactions between the *A*O$_8$ and *B*O$_6$ polyhedra in the *I*2/*a* fergusonite structure leads to changes in the unit cell volume.

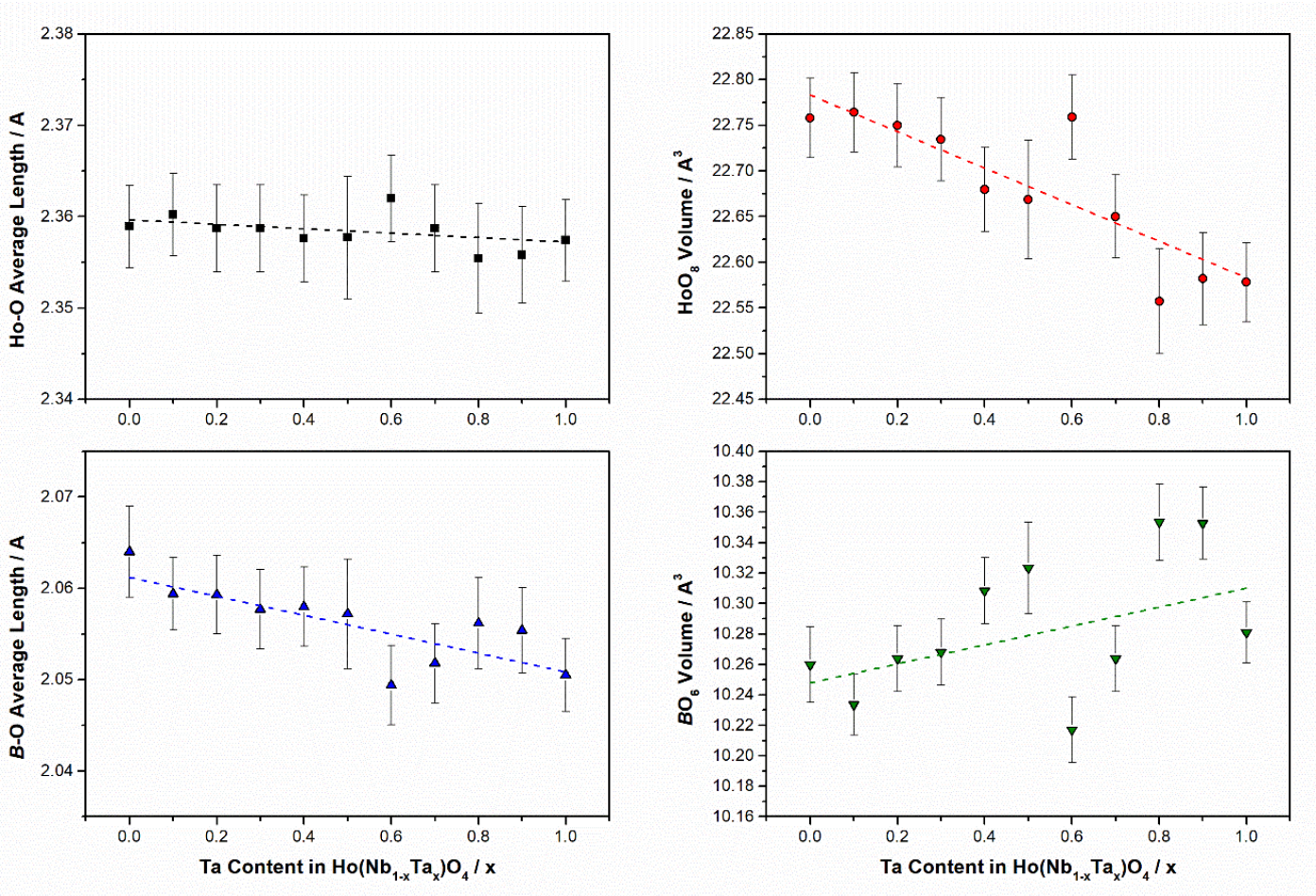

Figure 11: Compositional dependence of the Ho-O and *B*-O average bond lengths, as well as HoO$_8$ and *B*O$_6$ polyhedra volume in the Ho(Nb$_{1-x}$Ta$_x$)O$_4$ series.

To better understand the variation in the polyhedra volume, the individual bond lengths are plotted in Figure 12. Interestingly, it appears that the longest Ho-O and *B*-O bonds act contrary to the shorter bonds. As the Ta content (x) increases, the Ho-O(2)$_L$ bond length increases, and the shorter bonds decrease. On the *B*-site, the opposite trend is observed – the *B*-O(2)$_L$ bond decreases in length as the shorter bond lengths increase. A similar effect was observed by Shimakawa *et al.* in the $SrBi_2(Ta_{1-x}Nb_x)O_9$ Aurivillius phases, where the shorter (Nb/Ta)-O bonds increased whilst the longer (Nb/Ta)-O bonds decreased in length with increasing Ta content.[47] This occurred whilst the average (Nb/Ta)-O bond distance remained relatively constant across the series. These authors argued that this was a consequence of the difference in covalency between Nb^V and Ta^V. As the Ta(5*d*) orbital is radially extended further than the Nb(4*d*) orbital, hybridization with the O(2*p*) orbitals is enhanced, resulting in a shorter *B*-O(2)$_L$ bond length. The antagonistic effect evident in Figure 12 highlights the importance of the long *B*-O contacts in *I*2/*a* fergusonite structured oxides,[28, 31] and further supports our earlier work on the $Ln(Nb_{1-x}Ta_x)O_4$ series (*Ln* = Sm, Ho) where ground state energy calculations identified the covalent nature of the long *B*-O contacts.[16]

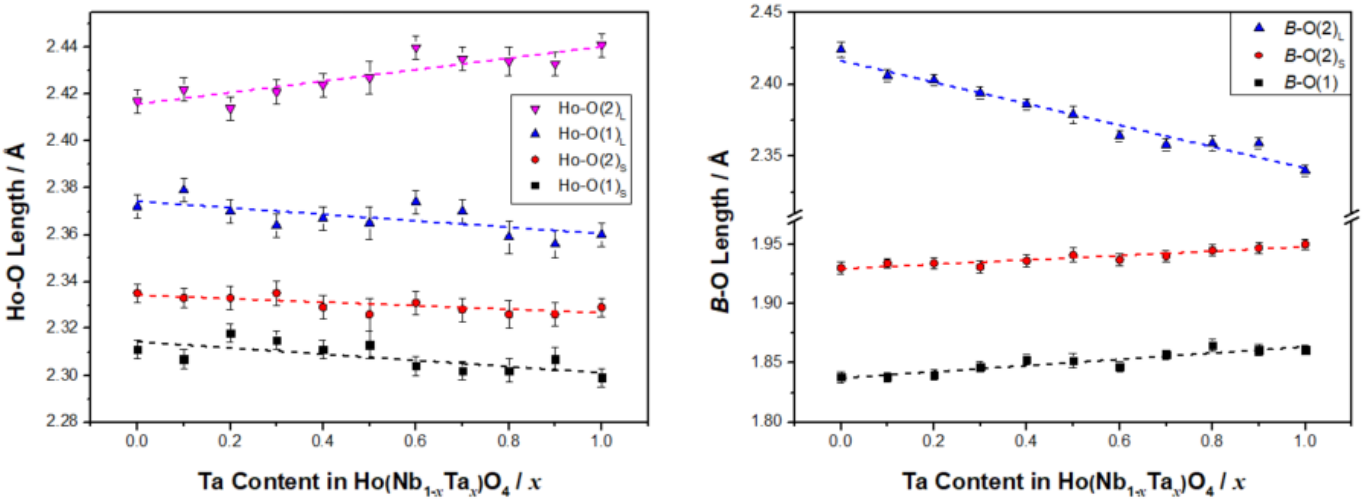

Figure 12: Composition dependence of the Ho-O and *B*-O bond lengths in the $Ho(Nb_{1-x}Ta_x)O_4$ series. Where not apparent, the errors are smaller than the symbols. For definition of O(1) and O(2) see Table S1 of the ESI.

The structural refinements using combined SXRD and NPD datasets reveal a movement of the *B*-site from the center of the polyhedra. Figure 13 demonstrates that as Ta is substituted for Nb, there is a systematic increase in the y atomic positional parameter of the *B*-site cation. This shift shortens the long B-O(2)$_L$ distance resulting in a stronger bonding interaction. Similar effects have also been observed by Lufaso *et al.*, with an out-of-center distortion present in (Nb/Ta)O_6 octahedra in some perovskites as a consequence of a second-order Jahn-Teller effect.[46]

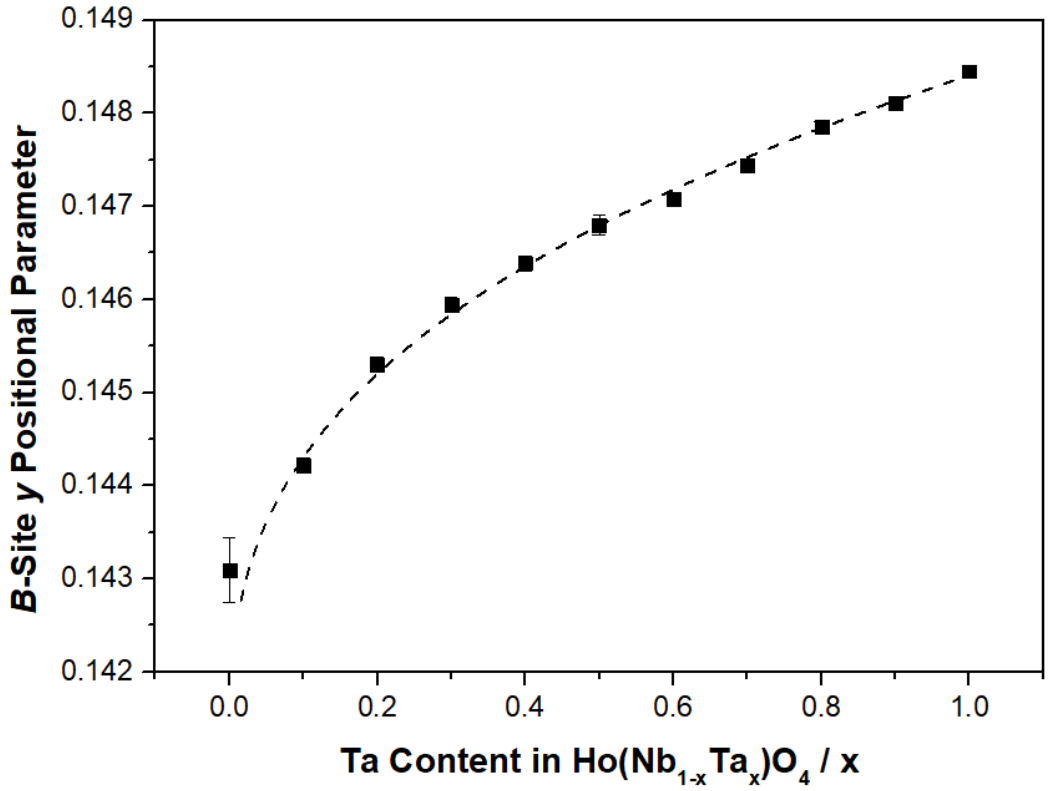

Figure 13: Composition dependence of the *B*-site *y* atomic positional parameter in the $Ho(Nb_{1-x}Ta_x)O_4$ series. Where not apparent, the errors are smaller than the symbols. Dashed line is drawn to guide the eye.

The difference in covalency of the Nb-O and Ta-O bonds and the displacement of the *B*-site cation are thought to account for the change in the temperature of the *I*2/*a* to *I*4$_1$/*a* phase transition between the niobates and tantalates. Studies of *Ln*NbO_4 and *Ln*TaO_4 have demonstrated a significant disparity between the phase transition temperature of the two structures.[28, 38] We recently showed that a Γ_2^+ distortion mode describes the displacements of the cations from their equivalent high symmetry (tetragonal scheelite) positions and this can be used as an order parameter for the transition. As described by Arulnesan *et al.*, this phase transition involves the breaking of the long Nb-$O(2)_L$ bonds in the distorted NbO_6 polyhedra to form NbO_4 tetrahedra.[31] Auckett *et al.* recently demonstrated that chemical substitution in the $La(Nb_{1-x}Mo_x)O_{4+\delta}$ series could also break the longer Nb-$O(2)_L$ bonds to transition from the *I*2/*a* to the *I*4$_1$/*a* structure.[22] David noted the competition between Nb^V and Ta^V to occupy either tetrahedra or distorted octahedra in Nd*B*O_4 (*B* = Nb, Ta).[40] In particular, Nb^V has a smaller displacement from the center of the tetrahedra than Ta^V. This is schematically shown in Figure 14. Evidently the increased displacement of the Ta cation compared to the Nb cation results in a stronger Ta-$O(2)_L$ bond and higher transition temperature.

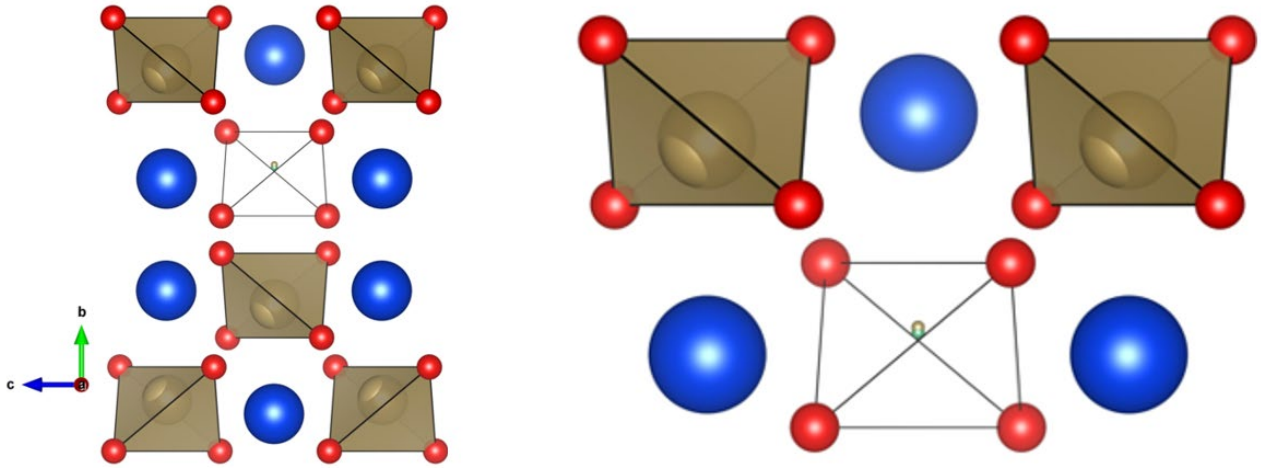

Figure 14: The Ho(Nb/Ta)O_4 fergusonite (*I*2/*a*) structure, with (Nb/Ta)O_4 tetrahedra, rather than octahedra drawn in brown for clarity. The Ho cations (blue spheres) and oxygen anions (red spheres) are also depicted. In the unshaded (Nb/Ta)O_4 tetrahedra, the size of the Nb and Ta cations has been reduced to illustrate the shift in position within the tetrahedra. The Ta^V cations (brown spheres) are more displaced than the Nb^V cations (green sphere).

In summary, a combined SXRD and NPD study has been used to accurately determine the bond lengths and atomic positions of the cations and anions in the Ho($Nb_{1-x}Ta_x$)O_4 series. This has revealed a change in the (Nb/Ta)-O bond lengths, reflective of the difference in valence *d* orbitals, with an additional strengthening of the longer *B*-$O(2)_L$ bonds upon substitution by the Ta cation with its more extended *d* orbitals. As this long bond contact is important in the *I*2/*a* to $I4_1/a$ phase transition, this potentially explains why Ta-containing oxides have a much higher phase transition temperature than their isostructural niobates. However, it remains unclear whether the differences between $HoNbO_4$ and $HoTaO_4$ are driven by structural differences, or by differences in electronics.

(iv) *Partial Density of State Calculations Using Density Functional Theory*

To understand the differences in the electronics of Nb and Ta, the partial density of states (pDoS) of elemental Nb and Ta were first calculated (see Figure S3 of the ESI), with the elemental form of each metal crystallizing in the space group $Im\bar{3}m$ (#229) with lattice parameters of 3.320 and 3.322 Å respectively. Slight differences were observed in the structure of the conduction band evident in the two pDoS plots.

The density of states (DoS) of $HoNbO_4$ and $HoTaO_4$ were also examined using DFT, where the experimentally determined structural parameters from the combined SXRD and NPD refinements were treated as input parameters (Figure 15). In both compounds, the electronic structure analysis shows that the O(*p*) states dominate the valence bands, and the Nb/Ta(*d*) states dominate the conduction bands. The calculations highlight a difference in band gap between $HoNbO_4$ and $HoTaO_4$, with the band gap being larger in the tantalate than in the corresponding niobate. This was experimentally observed using UV-Vis spectroscopy (see Figure S5 of the ESI). This does not, however, allow us to decouple between the structural and electronic effects.

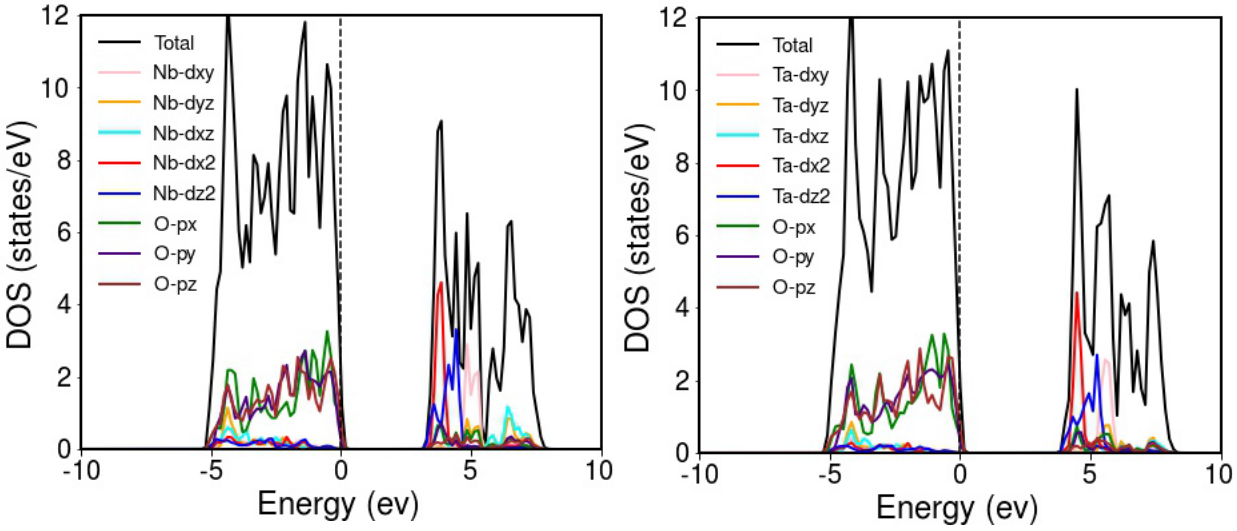

Figure 15: The partial and total density of states of (Left) $HoNbO_4$ and (Right) $HoTaO_4$ in the isostructural *I*2/*a* space group.

The pDoS of both $HoNbO_4$ and $HoTaO_4$, show different broadening of the d_{x2-y2} and d_{z2} orbital contribution. This is consistent with a change in the distorted $(Nb/Ta)O_6$ coordination environment. Calculations were then undertaken for three additional $LnNbO_4$ (*Ln* = Pr, Gd, Yb) oxides. These showed that the broadening of the e_g state is not significantly impacted by the choice of *Ln* cation, nor is the calculated band gap. This reflects the 'core-like' non-bonding nature of the *Ln*(4*f*) electrons. In an attempt to decouple the structural and electronic effects, the calculations for $HoNbO_4$ were repeated but with the Nb artificially replaced by Ta – that is the $HoNbO_4$ structure was imposed on $HoTaO_4$. These calculations resulted in an increase in the band gap revealing the significant different contribution of the 4*d* and 5*d* valence orbitals is the major driver for the differences between the niobates and tantalates (Figure 16).

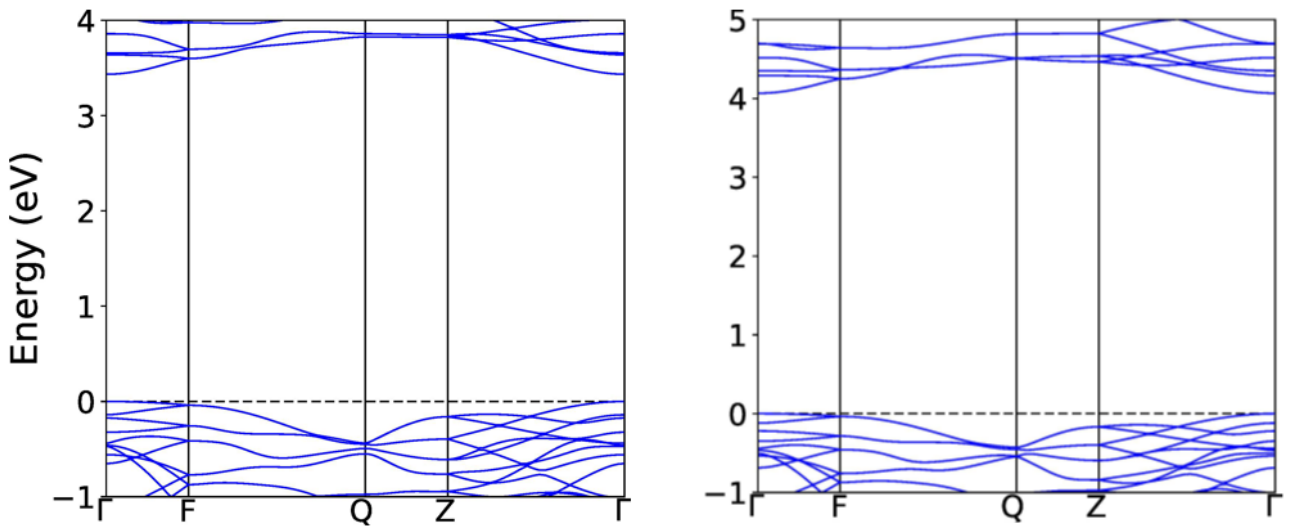

Figure 16: The electronic band structure of (Left) $HoNbO_4$ and (Right) $HoTaO_4$ with Ta replacing Nb, along the high-symmetry path G-F-Q-Z-G.

To determine whether any electronic changes were present across the different *Ln*TaO_4 structures, the DoS were also compared between the $PrTaO_4$ ($P2_1/c$), $GdTaO_4$ ($I2/a$), and $YbTaO_4$ ($P2/c$) structures. Comparatively, there are significant changes in the structure of the conduction band, highlighting changes in the electronic structure as the crystal structure changes (Figure S4). Interestingly, the band gap of the tantalate compounds is consistently larger than the corresponding niobate, suggesting this is a result of the difference in electronic structure between Nb and Ta.

Conclusions

The present work provides accurate structures of the *Ln*TaO_4 metal oxides synthesized by a solid-state reaction at 1400 °C. The *Ln*TaO_4 samples crystallize into different monoclinic structures depending on the size of the *Ln* cation. The larger *Ln* cations (*Ln* = La, Pr) crystallize in the $P2_1/c$ space group, the intermediate *Ln* cations (*Ln* = Nd-Tb) crystallize in the $I2/a$ space group, and the smaller *Ln* cations (*Ln* = Dy-Lu) crystallize in the $P2/c$ space group. The decrease in unit cell volume going across the series from *Ln* = Nd to Tb correlates with a decrease in the volume of the *Ln*O_8 polyhedra due to the changing size of the *Ln* cation as the 4*f* orbitals are progressively filled. Bond valence sum calculations show that the Ta cations are best described as six-coordinate in all three structural types. The distortion of the TaO_6 polyhedra in the fergusonite-type ($I2/a$) structures is similar to that seen in the isostructural *Ln*NbO_4 niobates. These six-coordinate distorted polyhedra consist of four shorter (~1.9 Å) bonds and two longer (~2.4 Å) bonds. This work demonstrated the ability to isolate pure samples of *Ln*TaO_4 oxides with both the $P2/c$ or $I2/a$ structure based on the final heating temperature, and that this is correlated with the $I2/a$ to $I4_1/a$ phase transition temperature. This demonstrates that the structure of the *AB*O_4 metal oxides is not purely driven by the steric effects or by the r_A/r_O and r_B/r_O ionic radii ratios.

In the *I*2/*a* structures, the unit cell volume of the tantalates was observed to be systematically smaller than that of the corresponding isostructural niobate. Substitution of Nb for Ta in the $Ln(Nb_{1-x}Ta_x)O_4$ solid solutions revealed differences. For $Pr(Nb_{1-x}Ta_x)O_4$, the *I*2/*a* to $P2_1/c$ phase transition occurred suddenly, with the $P2_1/c$ structure only observed for the end member ($PrTaO_4$, $x = 1.0$). This is in contrast with the $Ln(Nb_{1-x}Ta_x)O_4$ (*Ln* = Dy, Ho, Yb, Lu) series, where the phase transition appeared more gradual with two-phase regions observed around $x = 0.8$. The composition-induced reduction in the unit cell volumes was found to be dependent on the lanthanoid, indicating there is an interaction between the AO_8 and BO_6 sublattices. This effect appears to be unique to the fergusonite structure, with a comparative study of some pyrochlore oxides not revealing such a relationship.

The impact of gradual Ta doping in $Ho(Nb_xTa_{1-x})O_4$ was further studied using a combination of SXRD and NPD. The average Ho-O and *B*-O bond distances were invariant of the Ta content. However, inspection of the individual bond lengths reveals shortening of the *B*-O(2) long bond due to the greater hybridization of the Ta(5*d*) and O(2*p*) orbitals. This indicates that the *B*-O(2) long bond, which is important to the *I*2/*a* to $I4_1/a$ phase transition, is stronger in the tantalum-containing fergusonites than the corresponding niobates. This further explains why the phase transition in the Ta-containing $LnTaO_4$ structures occurs at a significantly higher temperature than in the isostructural $LnNbO_4$. This is powerful demonstration of the role of both the ionic radii and the electronic structure of the cations in governing the crystal structure of complex oxides. The extent in which the electronics influence the crystal structure however remains unclear, with pDoS calculations indicating differences in band gaps between the $LnNbO_4$ and $LnTaO_4$ structures. It is hoped that this work will inspire others to look closely at these subtle differences.

Acknowledgements

BJK acknowledges the support of the Australian Research Council for this work that was facilitated by access to Sydney Analytical, a core research facility at the University of Sydney. BGM acknowledges the Australian Institute for Nuclear Science and Engineering for a PGRA scholarship. Part of this work was undertaken at the powder diffraction beamline at the Australian Synchrotron. MSM acknowledges the financial support from the Comunidad de Madrid, Spain, through an "Atracción de Talento Investigador" fellowship (2020-T2/IND-20581). SM acknowledges DRDO, India, through ACRHEM (DRDO/18/1801/2016/01038: ACRHEM-PHASE-III). GV acknowledges UoH-IoE-RC3-21-046 for funding and CMSD University of Hyderabad for providing the computational facility. SM thanks Ms. Anuroopa Behatha from IIT Hyderabad for technical help.

References

1. Liu, X.; Gu, S.; Zhao, Y.; Zhou, G.; Li, W., $BiVO_4$, Bi_2WO_6 and Bi_2MoO_6 photocatalysis: A brief review. *Journal of Materials Science & Technology* **2020,** *56*, 45-68.
2. Potanina, E. A.; Orlova, A. I.; Mikhailov, D. A.; Nokhrin, A. V.; Chuvil'deev, V. N.; Boldin, M. S.; Sakharov, N. V.; Lantcev, E. A.; Tokarev, M. G.; Murashov, A. A., Spark Plasma Sintering of fine-grained $SrWO_4$ and $NaNd(WO_4)_2$ tungstates ceramics with the scheelite structure for nuclear waste immobilization. *Journal of Alloys and Compounds* **2019,** *774*, 182-190.
3. Afif, A.; Zaini, J.; Rahman, S. M. H.; Eriksson, S.; Islam, M. A.; Azad, A. K., Scheelite type $Sr_{1-x}Ba_xWO_4$ (x = 0.1, 0.2, 0.3) for possible application in Solid Oxide Fuel Cell electrolytes. *Scientific Reports* **2019,** *9* (1), 9173.
4. Bastide, J., Simplified systematics of the compounds ABX_4 ($X = O^{2-}$, F^-) and possible evolution of their crystal-structures under pressure. *Journal of Solid State Chemistry* **1987,** *71* (1), 115-120.
5. Errandonea, D.; Manjón, F. J., Pressure effects on the structural and electronic properties of ABX_4 scintillating crystals. *Progress in Materials Science* **2008,** *53* (4), 711-773.
6. Murphy, G. L.; Kennedy, B. J.; Kimpton, J. A.; Gu, Q.; Johannessen, B.; Beridze, G.; Kowalski, P. M.; Bosbach, D.; Avdeev, M.; Zhang, Z., Nonstoichiometry in strontium uranium oxide: Understanding the rhombohedral–orthorhombic transition in $SrUO_4$. *Inorganic Chemistry* **2016,** *55* (18), 9329-9334.
7. Injac, S.; Yuen, A. K. L.; Avdeev, M.; Wang, C.-H.; Turner, P.; Brand, H. E. A.; Kennedy, B. J., Structural and magnetic studies of ABO_4-type ruthenium and osmium oxides. *Inorganic Chemistry* **2020,** *59* (5), 2791-2802.
8. Injac, S.; Yuen, A. K.; Avdeev, M.; Orlandi, F.; Kennedy, B. J., Structural and magnetic studies of $KOsO_4$, a $5d^1$ quantum magnet oxide. *Physical Chemistry Chemical Physics* **2019,** *21* (14), 7261-7264.
9. Peixoto, J. C.; Dias, A.; Matinaga, F. M.; Siqueira, K. P. F., Luminescence properties of $PrNbO_4$ and $EuNbO_4$ orthoniobates and investigation of their structural phase transition by high-temperature Raman spectroscopy. *Journal of Luminescence* **2021,** *238*, 118284.
10. Liu, T.; Zhang, X.; Guan, J.; Catlow, C. R. A.; Walsh, A.; Sokol, A. A.; Buckeridge, J., Insight into the Fergusonite–Scheelite Phase Transition of ABO_4-Type Oxides by Density Functional Theory: A Case Study of the Subtleties of the Ground State of $BiVO_4$. *Chemistry of Materials* **2022,** *34* (12), 5334-5343.
11. Vats, B. G.; Shafeeq, M.; Kesari, S., Triple molybdates and tungstates scheelite structures: Effect of cations on structure, band-gap and photoluminescence properties. *Journal of Alloys and Compounds* **2021,** *865*, 158818.
12. Gan, Y.; Liu, W.; Zhang, W. T.; Li, W. J.; Huang, Y.; Qiu, K. H., Effects of Gd_{3+} codoping on the enhancement of the luminescent properties of a $NaBi(MoO_4)_2$:Eu^{3+} red-emitting phosphors. *Journal of Alloys and Compounds* **2019,** *784*, 1003-1010.
13. Hill, C.; Weber, M. C.; Lehmann, J.; Leinen, T.; Fiebig, M.; Kreisel, J.; Guennou, M., Role of the ferroelastic strain in the optical absorption of $BiVO_4$. *APL Materials* **2020,** *8* (8), 081108.
14. Guo, D.; Zhou, D.; Li, W.-B.; Pang, L.-X.; Dai, Y.-Z.; Qi, Z.-M., Phase evolution, crystal structure, and microwave dielectric properties of water-insoluble $(1 - x)LaNbO_4 - xLaVO_4$ ($0 \le x \le 0.9$) ceramics. *Inorganic Chemistry* **2017,** *56* (15), 9321-9329.
15. Ferguson, R. B., The crystallography of synthetic $YTaO_4$ and fused fergusonite. *The Canadian Mineralogist* **1957,** *6* (1), 72-77.
16. Mullens, B. G. A., M.; Brand, H. E. A.; Mondal, S.; Vaitheeswaran, G.; Kennedy, B. J.; , Insights into the structural variations in $SmNb_{1-x}Ta_xO_4$ and $HoNb_{1-x}Ta_xO_4$ combined experimental and computational studies. *Dalton Transactions* **2021,** *50*, 9103-9117.
17. Bayliss, R. D.; Pramana, S. S.; An, T.; Wei, F.; Kloc, C. L.; White, A. J. P.; Skinner, S. J.; White, T. J.; Baikie, T., Fergusonite-type $CeNbO_{4+\delta}$: Single crystal growth, symmetry revision and conductivity. *Journal of Solid State Chemistry* **2013,** *204*, 291-297.
18. Fulle, K.; McMillen, C. D.; Sanjeewa, L. D.; Kolis, J. W., Hydrothermal chemistry and growth of fergusonite-type $RENbO_4$ (*RE* = La–Lu, Y) single crystals and new niobate hydroxides. *Crystal Growth & Design* **2016,** *16* (9), 4910-4917.

19. Toyoura, K.; Sakakibara, Y.; Yokoi, T.; Nakamura, A.; Matsunaga, K., Oxide-ion conduction via interstitials in scheelite-type $LaNbO_4$: A first-principles study. *Journal of Materials Chemistry A* **2018,** *6* (25), 12004-12011.
20. Pramana, S. S.; Baikie, T.; An, T.; Tucker, M. G.; Wu, J.; Schreyer, M. K.; Wei, F.; Bayliss, R. D.; Kloc, C. L.; White, T. J.; Horsfield, A. P.; Skinner, S. J., Correlation of local structure and diffusion pathways in the modulated anisotropic oxide ion conductor $CeNbO_{4.25}$. *Journal of the American Chemical Society* **2016,** *138* (4), 1273-1279.
21. Ferrara, C. M., A.; Ritter, C.; Malavasi, L.; Tealdi, C.; , Interstitial oxide ion migration in scheelite-type electrolytes: A combined neutron diffraction and computational study. *Journal of Materials Chemistry A* **2015,** *3*, 22258-22265.
22. Auckett, J. E.; Lopez-Odriozola, L.; Clark, S. J.; Evans, I. R., Exploring the nature of the fergusonite-scheelite phase transition and ionic conductivity enhancement by Mo^{6+} doping in $LaNbO_4$. *Journal of Materials Chemistry A* **2021,** *9* (7), 4091-4102.
23. Canu, G.; Giannici, F.; Chiara, A.; Confalonieri, G.; Longo, A.; Buscaglia, M. T.; Dapiaggi, M.; Buscaglia, V.; Martorana, A., Characterisation of scheelite $LaW_{0.16}Nb_{0.84}O_{4.08}$ ion conductor by combined synchrotron techniques: Structure, W oxidation state and interdiffusion. *Journal of Alloys and Compounds* **2021,** *857*.
24. Garg, A. B.; Errandonea, D.; Rodríguez-Hernández, P.; Muñoz, A., High-pressure monoclinic–monoclinic transition in fergusonite-type $HoNbO_4$. *Journal of Physics: Condensed Matter* **2021,** *33* (19), 195401.
25. Sarin, P.; Hughes, R. W.; Lowry, D. R.; Apostolov, Z. D.; Kriven, W. M., High-temperature properties and ferroelastic phase transitions in rare-earth niobates ($LnNbO_4$). *Journal of the American Ceramic Society* **2014,** *97* (10), 3307-3319.
26. Titov, Y. A.; Sych, A. M.; Sokolov, A. N.; Kapshuk, A. A.; Markiv, V. Y.; Belyavina, N. M., Crystal structure of the high-pressure modification of $NdTaO_4$. *Journal of Alloys and Compounds* **2000,** *311* (2), 252-255.
27. Wang, X. N.; Wang, B. Y.; Tan, D. Y.; Xiao, W. S.; Song, M. S., Phase transformations of zircon-type $DyVO_4$ at high pressures up to 36.4 GPa: X-ray diffraction measurements. *Journal of Alloys and Compounds* **2021,** *875*.
28. Saura Múzquiz, M.; Mullens, B. G.; Maynard-Casely, H. E.; Kennedy, B. J., Neutron diffraction study of the monoclinic-tetragonal phase transition in $NdNbO_4$ and $NdTaO_4$. *Dalton Transactions* **2021,** *50*, 11485-11497.
29. Siqueira, K. P.; Dias, A., Effect of the processing parameters on the crystalline structure of lanthanide orthotantalates. *Materials Research* **2014,** *17*, 167-173.
30. Haugsrud, R.; Norby, T., Proton conduction in rare-earth ortho-niobates and ortho-tantalates. *Nature Materials* **2006,** *5* (3), 193-196.
31. Arulnesan, S. W.; Kayser, P.; Kimpton, J. A.; Kennedy, B. J., Studies of the fergusonite to scheelite phase transition in $LnNbO_4$ orthoniobates. *Journal of Solid State Chemistry* **2019,** *277*, 229-239.
32. Machida, M.; Murakami, S.; Kijima, T.; Matsushima, S.; Arai, M., Photocatalytic property and electronic structure of lanthanide tantalates, $LnTaO_4$ (*Ln* = La, Ce, Pr, Nd, and Sm). *The Journal of Physical Chemistry B* **2001,** *105* (16), 3289-3294.
33. Siqueira, K. P. F.; Carmo, A. P.; Bell, M. J. V.; Dias, A., Optical properties of undoped $NdTaO_4$, $ErTaO_4$ and $YbTaO_4$ ceramics. *Journal of Luminescence* **2016,** *179*, 146-153.
34. Shannon, R. D., Revised effective ionic radii and systematic studies of interatomic distances in halides and chalcogenides. *Acta crystallographica section A: crystal physics, diffraction, theoretical and general crystallography* **1976,** *32* (5), 751-767.
35. Brunckova, H.; Kolev, H.; Rocha, L. A.; Nassar, E. J.; Moscardini, S. B.; Medvecky, L., XPS characterization and luminescent properties of $GdNbO_4$ and $GdTaO_4$ thin films. *Applied Surface Science* **2020,** *504*, 144358.

36. Brunckova, H.; Mudra, E.; Medvecky, L.; Kovalcikova, A.; Durisin, J.; Sebek, M.; Girman, V., Effect of lanthanides on phase transformation and structural properties of *Ln*NbO_4 and *Ln*TaO_4 thin films. *Materials & Design* **2017,** *134*, 455-468.
37. Haugsrud, R.; Norby, T., High-temperature proton conductivity in acceptor-substituted rare-earth ortho-tantalates, *Ln*TaO_4. *Journal of the American Ceramic Society* **2007,** *90* (4), 1116-1121.
38. Stubičan, V. S., High-temperature transitions in rare-earth niobates and tantalates. *Journal of the American Ceramic Society* **1964,** *47* (2), 55-58.
39. David, W. I. F., The high-temperature paraelastic structure of $LaNbO_4$. *Materials Research Bulletin* **1983,** *18* (6), 749-756.
40. David, W. I. F., Transition temperature - Spontaneous strain - Atomic displacement relationships in ferroelastics. *Materials Research Bulletin* **1983,** *18* (7), 809-816.
41. Farid, U.; Khan, H. U.; Avdeev, M.; Injac, S.; Kennedy, B. J., Structural studies of the high temperature phases of $AgTaO_3$. *Journal of Solid State Chemistry* **2018,** *258*, 859-864.
42. Farid, U.; Khan, H. U.; Avdeev, M.; Whittle, T. A.; Kennedy, B. J., Preparation and high resolution structural studies of $Li_xAg_{1-x}NbO_3$ lead free piezoelectrics. *Journal of Solid State Chemistry* **2019,** *269*, 401-408.
43. Kennedy, B. J.; Prodjosantoso, A. K.; Howard, C. J., Powder neutron diffraction study of the high temperature phase transitions in $NaTaO_3$. *Journal of Physics: Condensed Matter* **1999,** *11* (33), 6319-6327.
44. Megaw, H. D., The seven phases of sodium niobate. *Ferroelectrics* **1974,** *7* (1), 87-89.
45. Peel, M. D.; Thompson, S. P.; Daoud-Aladine, A.; Ashbrook, S. E.; Lightfoot, P., New twists on the perovskite theme: Crystal structures of the elusive phases *R* and *S* of $NaNbO_3$. *Inorganic Chemistry* **2012,** *51* (12), 6876-6889.
46. Lufaso, M. W., Crystal structures, modeling, and dielectric property relationships of 2:1 ordered $Ba_3MM'_2O_9$ (*M* = Mg, Ni, Zn; *M'* = Nb, Ta) perovskites. *Chemistry of Materials* **2004,** *16* (11), 2148-2156.
47. Shimakawa, Y.; Kubo, Y.; Tauchi, Y.; Kamiyama, T.; Asano, H.; Izumi, F., Structural distortion and ferroelectric properties of $SrBi_2(Ta_{1-x}Nb_x)_2O_9$. *Applied Physics Letters* **2000,** *77* (17), 2749-2751.
48. Das, P. R.; Biswal, L.; Behera, B.; Choudhary, R. N. P., Structural and electrical properties of $Na_2Pb_2Eu_2W_2Ti_4X_4O_{30}$ (*X*=Nb, Ta) ferroelectric ceramics. *Materials Research Bulletin* **2009,** *44* (6), 1214-1218.
49. Subramanian, M. A.; Aravamudan, G.; Subba Rao, G. V., Oxide pyrochlores — A review. *Progress in Solid State Chemistry* **1983,** *15* (2), 55-143.
50. Mullens, B. G.; Zhang, Z.; Avdeev, M.; Brand, H. E. A.; Cowie, B. C. C.; D'Angelo, A.; Múzquiz, M. S.; Kennedy, B. J., Average and local ordering of $Yb_2(Ti_{2-x}Yb_x)O_{7-x/2}$ 'stuffed' pyrochlores: The development of a robust structural model. *Journal of Solid State Chemistry* **2021,** *302*, 122412.
51. Mullens, B. G.; Zhang, Z.; Avdeev, M.; Brand, H. E. A.; Cowie, B. C. C.; Saura Múzquiz, M.; Kennedy, B. J., Effect of long- and short-range disorder on the oxygen ionic conductivity of $Tm_2(Ti_{2-x}Tm_x)O_{7-x/2}$ "stuffed" pyrochlores. *Inorganic Chemistry* **2021,** *60* (7), 4517-4530.
52. Wallwork, K. S.; Kennedy, B. J.; Wang, D. In *The high resolution powder diffraction beamline for the Australian Synchrotron*, AIP Conference Proceedings, American Institute of Physics: 2007; pp 879-882.
53. Avdeev, M.; Hester, J. R., ECHIDNA: a decade of high-resolution neutron powder diffraction at OPAL. *Journal of Applied Crystallography* **2018,** *51* (6), 1597-1604.
54. Coelho, A. A., TOPAS and TOPAS-Academic: an optimization program integrating computer algebra and crystallographic objects written in C++. *Journal of Applied Crystallography* **2018,** *51* (1), 210-218.
55. Momma, K.; Izumi, F., VESTA 3 for three-dimensional visualization of crystal, volumetric and morphology data. *Journal of applied crystallography* **2011,** *44* (6), 1272-1276.
56. Hohenberg, P.; Kohn, W., Inhomogeneous electron gas. *Physical Review B* **1964,** *136* (3B), B864.
57. Kohn, W.; Sham, L. J., Self-consistent equations including exchange and correlation effects. *Physical Review* **1965,** *140* (4A), 1133.
58. Blochl, P. E., Projector augmented-wave method. *Physical Review B* **1994,** *50* (24), 17953-17979.
59. Perdew, J. P.; Burke, K.; Ernzerhof, M., Generalized gradient approximation made simple. *Physical Review Letters* **1996,** *77* (18), 3865-3868.

60. Perdew, J. P.; Ruzsinszky, A.; Csonka, G. I.; Vydrov, O. A.; Scuseria, G. E.; Constantin, L. A.; Zhou, X. L.; Burke, K., Restoring the density-gradient expansion for exchange in solids and surfaces. *Physical Review Letters* **2008,** *100* (13), 136406.
61. Monkhorst, H. J.; Pack, J. D., Special points for brillouin-zone integrations. *Physical Review B* **1976,** *13* (12), 5188-5192.
62. Fischer, T. H.; Almlof, J., General-methods for geometry and wave-function optimization. *Journal of Physical Chemistry* **1992,** *96* (24), 9768-9774.
63. Brixner, L. H.; Chen, H. y., On the structural and luminescent properties of the *M'-Ln*TaO_4 rare earth tantalates. *Journal of The Electrochemical Society* **1983,** *130* (12), 2435-2443.
64. Roth, R. S.; Negas, T.; Parker, H. S.; Minor, D. B.; Jones, C., Crystal chemistry of cerium titanates, tantalates and niobates. *Materials Research Bulletin* **1977,** *12* (12), 1173-1182.
65. Rooksby, H.; White, E., The structures of 1:1 compounds of rare earth oxides with niobia and tantala. *Acta Crystallographica* **1963,** *16* (9), 888-890.
66. Wakeshima, M.; Nishimine, H.; Hinatsu, Y., Crystal structures and magnetic properties of rare earth tantalates RE_3TaO_7 (*RE*= rare earths). *Journal of Physics: Condensed Matter* **2004,** *16* (23), 4103.
67. Zhou, Q.; Saines, P. J.; Sharma, N.; Ting, J.; Kennedy, B. J.; Zhang, Z.; Withers, R. L.; Wallwork, K. S., Crystal structures and phase transitions in A-site deficient perovskites $Ln_{1/3}TaO_3$. *Chemistry of Materials* **2008,** *20* (21), 6666-6676.
68. Langenbach-Kuttert, B.; Sturm, J.; Gruehn, R., Zur darstellung und struktur von $LaTa_3O_9$ röntgenographische und elektronenmikroskopische untersuchungen. *Zeitschrift für anorganische und allgemeine Chemie* **1987,** *548* (5), 33-44.
69. Hartenbach, I.; Lissner, F.; Nikelski, T.; Meier, S. F.; Müller-Bunz, H.; Schleid, T., Über oxotantalate der lanthanide des formeltyps *M*TaO_4 (*M* = La–Nd, Sm–Lu). *Zeitschrift für anorganische und allgemeine Chemie* **2005,** *631* (12), 2377-2382.
70. Korzeniowski, K.; Sobczyk, M., A study of optical properties of Sm^{3+}-doped *M'*-type structure $YTaO_4$ powders synthesized by the disodium tetraborate flux method. *Journal of Alloys and Compounds* **2018,** *753*, 717-724.
71. Popovici, E.-J.; Nazarov, M.; Muresan, L.; Noh, D. Y.; Tudoran, L. B.; Bica, E.; Indrea, E., Synthesis and characterisation of terbium activated yttrium tantalate phosphor. *Journal of Alloys and Compounds* **2010,** *497* (1), 201-209.
72. Wang, J.; Chong, X.; Zhou, R.; Feng, J., Microstructure and thermal properties of *RE*TaO_4 (*RE*=Nd, Eu, Gd, Dy, Er, Yb, Lu) as promising thermal barrier coating materials. *Scripta Materialia* **2017,** *126*, 24-28.
73. Tsunekawa, S.; Kamiyama, T.; Asano, H.; Fukuda, T., Relationship between covalence and displacive phase transition temperature in *RA*O_4 and $LiAO_3$ (*R* = rare-earth element and *A* = Nb and Ta). *Journal of Solid State Chemistry* **1995,** *116* (1), 28-32.
74. Brese, N.; O'keeffe, M., Bond-valence parameters for solids. *Acta Crystallographica Section B: Structural Science* **1991,** *47* (2), 192-197.
75. Kennedy, B. J.; Avdeev, M., The structure of *C*-type Gd_2O_3. A powder neutron diffraction study using enriched ^{160}Gd. *Australian Journal of Chemistry* **2011,** *64* (1), 119-121.
76. Whittaker, E.; Muntus, R., Ionic radii for use in geochemistry. *Geochimica et Cosmochimica Acta* **1970,** *34* (9), 945-956.
77. Barnes, P. W.; Lufaso, M. W.; Woodward, P. M., Structure determination of A_2M^{3+} TaO6 and A_2M^{3+} NbO_6 ordered perovskites: octahedral tilting and pseudosymmetry. *Acta Crystallographica Section B: Structural Science* **2006,** *62* (3), 384-396.
78. Bukaemskiy, A. A.; Vinograd, V. L.; Kowalski, P. M., Ion distribution models for defect fluorite ZrO_2-$AO_{1.5}$ (*A* = *Ln*, Y) solid solutions: I. Relationship between lattice parameter and composition. *Acta Materialia* **2021,** *202*, 99-111.